CrossMark

Vertically Aligned Silicon Nanowire Array Decorated by Ag or Au Nanoparticles as SERS Substrate for Bio-molecular Detection

S. Chakraborti[1] · R. N. Basu[1] · S. K. Panda[1,2]

Abstract This review article summerises preparation techniques of vertically aligned silicon nanowire (Si NW) arrays through metal-assisted chemical etching (MacEtch) process and plasmonic nanoparticles (Ag and Au) with the perspective of the fabrication of surface-enhanced Raman scattering (SERS)-active substrates which are highly efficient for bio-molecular detection. At first, basic methods and mechanisms for SERS have been introduced and size and shape effects of the nanoparticles (NPs) on plasmonic vibration have been discussed. Comparative discussions on optical and plasmonic characteristics of Ag and Au NPs have also been presented in this section. Potential techniques for the synthesis of Ag and Au NPs with different sizes and shapes have been reported in the following section. Basic processes and mechanism for the fabrication of vertically aligned Si NW arrays on Si by MacEtch of Si wafer have been discussed. Template-assisted fabrication techniques for the vertically aligned Si NW arrays with controlled diameter and number density have also been reported. Finally, multifarious ways for the fabrication of SERS-active substrates by assembling noble metal NPs onto the NW surface have been discussed and their performance for bio-molecular detection has also been reported.

Introduction

Incidence of electromagnetic beam on metal/dielectric interface excites coherent oscillations of free electrons at the boundary which are often recognized as surface plasmons (SPs). The resonance (surface plasmon resonance) condition is established when the frequency of electromagnetic beam matches with the natural frequency of the free electron oscillation. Understanding of surface plasmon resonance (SPR) provides a design concept that guides the development of complex material structures with optimal optical properties. SPs are now being investigated for various application-oriented purposes which include photonics, magneto-optics, sensing of biological and chemical species, medical diagnosis, and environmental monitoring [1–5]. SPs, however, strongly depends on the size, shape, and environment of the surrounding metal body, enabling emerging research field like surface plasmon-based photonics or plasmonics. In case of low dimensional metal structures like quantum dots, nanoparticles (NPs), and nanorods, localized surface plasmon (LSP) excitation originates which can induce a strong enhancement of electromagnetic field in the near field region, leading to wide applications of plasmonic devices.

It is widely recognized that Raman signal can be enhanced by a factor of 10^6 to 10^8 using noble metal nanostructured substrates, termed as surface-enhanced Raman scattering, a LSP-based powerful analytical tool which has attracted great interest for the detection of wide range of adsorbate molecules because of its ultrahigh sensitivity down to the single-molecule

✉ R. N. Basu
rnbasu@cgcri.res.in

✉ S. K. Panda
sovan.panda@gmail.com

1 Fuel Cell and Battery Division, CSIR—Central Glass and Ceramic Research Institute, Kolkata 700032, India

2 Department of Electronics, Bidhan Chandra College, Rishra, Hooghly, West Bengal 712248, India

detection limit and amenability to molecular finger printing. Therefore, surface-enhanced Raman scattering (SERS) is being used in medical, chemical, and biological sciences and forensic sciences as a highly reliable and sensitive detector. More precisely, SERS has been used in detection of DNA, pesticides, nicotin, components of milk, glucose in blood, viruses, components of human urine, etc. [6–14]. Achievement of high selectivity, sensitivity, stability, and reproducibility are the major concerns for the fabrication of efficient SERS substrates. It is a common practice to use colloidal noble metal NPs as SERS substrates for the detection of inorganic or organic chemicals [15–18] but the inadequate particle number density and uncontrolled inter-particle distance limit the sensitivity and reproducibility in this technique. As an alternative, solid wafer-based SERS substrates have been thought of where a large number of metal NPs with desired size, shape, and inter-particle-spacing can be accommodated on wafer surface as monolayer which is beneficial to achieve coupled resonance and ultrahigh sensitivity as well. For SERS to occur efficiently, a molecule needs to be required in the close proximity of the mesoscopically occurred metal surface which supports electromagnetic resonance at the excitation/emission wavelength involved in the Raman scattering process. Therefore, it is advantageous to devise and fabricate an efficient and robust SERS substrate with satisfactory properties including, not limited to, (i) very high enhancement factor, (ii) stable, reproducibility, and uniformity, (iii) reusability, and (iv) surface functionalization to some targeted analytes. It has been reported that noble metal NPs exhibit a strong ultraviolet-visible (UV-VIS) absorption band due to LSP which is not present in the spectrum of the bulk metal [19–22]. Therefore, Ag and Au NP-assembled wafer-based SERS substrates have widely been studied which are sensitive in the UV-VIS region depending on the particle size and shape [23–27].

Number density, inter-particle distance, and shape of the noble metals estimate the enhancement factor and sensitivity as well of the wafer-based SERS-active substrates. The shape of the NPs is defined by the synthesis process parameters, and the particle number is additionally restricted by the flat surface area of the wafer (in case of monolayer dispersion) on which NPs get assembled. Thus, a flat wafer surface can accommodate limited number of NPs and the particle number can further be increased by fabricating one-dimensional (1D) nanostructures (NSs), standing vertically on the flat surface and attaching NPs on the surface of the 1D NSs since nanomaterials have very large surface to volume ratio as compared to bulk. Vertically aligned array of the 1D NSs, for example, nanorods (NRs) and nanotubes (NTs), are expected to have some more advantages which include larger surface area and efficient entry of liquid analytes (which are to be detected) through the space between the nanostructures of the array.

Vertically aligned silicon nanowire (Si NW) arrays are very imperative for the fabrication of such SERS substrate because they have very high surface area, excellent mechanical/chemical stability, and surface tailorability. Si NWs are one of a few stable nanomaterials which show excellent bio-compatibility, and in case of bio-molecular detection inside the living cells, these can be used efficiently to access the interior part of the cells because of their smaller diameter, high aspect ratio, and good mechanical strength. Qi et al. [28] compared the performance of vertically aligned and random NW array-based SERS substrates by measuring SERS intensity which showed superior performance of aligned NWs compared to random NWs. Therefore, alignment of NWs is quite significant for SERS-based device applications. High density and closely spaced Si NW array can be fabricated vertically by simple metal-assisted chemical etching (MacEtch) technique compared to the expensive vapor-liquid-solid (VLS) method leading to Si NWs a low-cost material for the fabrication of highly sensitive SERS substrate. In this review, we have focused on the synthesis of vertically aligned Si NW array and plasmonic NPs (Ag and Au) and fabrication of SERS-active substrates by assembling plasmonic NPs on the surface of Si. Application of these SERS-active substrates for bio-molecular sensing has also been reviewed since they show localized surface plasmon resonance (LSPR) in the UV-VIS region depending upon the size and shape of the NPs.

Method and Mechanisms

SERS is a phenomenon associated with the enhancement of the electromagnetic field surrounding small objects when optically excited near an intense and sharp plasmon resonance frequency. SERS predominantly originates from two basic methods: (i) electromagnetic enhancement and (ii) chemical enhancement. SERS mechanism is mainly dominated by electromagnetic enhancement in which Raman signal is enhanced by interaction of the electric field of the scattered wave with the induced electric field at the metal/dielectric interface due to SPR. Whereas, chemical enhancement takes place owing to the charge transfer through metal/dielectric interface causing an electric field at the interface which enhances the scattered beam intensity while electric field of the scattered photon interact with the interfacial electric field.

Electromagnetic Enhancement

Optical properties of bulk materials are characterized by their dielectric function (ε) which is related to the refractive index (n) by the following equation:

$$n(\omega) = \sqrt{\varepsilon(\omega)} \tag{1}$$

where both the $n(\omega)$ and $\varepsilon(\omega)$ are dependent on the frequency/wavelength of the incident radiation. For most of the optical

materials, dielectric constant and refractive index are positive real numbers. However, most often, dielectric function at a given wavelength is a complex number and the material is opaque. Metals are among the materials of complex dielectric constant having a real part ($Re[\varepsilon(\lambda)]$) related to the free electron concentration, and an imaginary part ($Im[\varepsilon(\lambda)]$) is attributed to the absorption of light. Dielectric function of real metal can be expressed as follows:

$$\varepsilon(\omega) = \varepsilon_\infty \left(1 - \frac{\omega_p{}^2}{\omega^2 + i\gamma_o\omega}\right) \qquad (2)$$

where ε_∞ and γ_0 are the optical response of the positive ions and damping in metal, respectively, and ω_p is the so-called plasma frequency of metals which is related to the electron concentration (n), permittivity in a vacuum (ε_o), and electronic charge (e) as follows:

$$\omega_p = \sqrt{\frac{ne^2}{m\varepsilon_o\varepsilon_\infty}} \qquad (3)$$

In the absence of an imaginary part, i.e., for non-absorbing metal, according to the lossless Drude model, the expression diminishes to the following:

$$\varepsilon(\omega) = \varepsilon_\infty \left(1 - \frac{\omega_p^2}{\omega^2}\right) = \varepsilon_\infty \left(1 - \frac{\lambda^2}{\lambda_p^2}\right) \qquad (4)$$

With decrease of free electron density in metal, plasmon absorption wavelength (λ_p) increases, which causes the red shift of plasmonic absorption band.

When metal surface is illuminated with light that is in resonance with the particle LSPR frequency, the EM enhancement is strong. To understand the field enhancement by electromagnetic means, let us consider the model comprised of single metal sphere with the diameter (r) smaller as compared to the wavelength of incident light. Let us also assume that the sphere is embedded in a medium of dielectric constant $_o$. The dielectric constant inside the metal sphere is denoted by $_i$ and the dielectric constant to be independent of the size of the sphere. Electric field of the incident electromagnetic wave (E), a vector that points along the z-axis, is uniformly distributed throughout the sphere. Metal polarizability (α) can be expressed as follows[29, 30]:

$$\alpha = gr^3 \qquad (5)$$

where

$$g = \frac{\varepsilon_i - \varepsilon_o}{\varepsilon_i + 2\varepsilon_o} \qquad (6)$$

Therefore, whenever the real part of $_i$ equals -2 $_o$ and the imaginary part is small, α becomes very large, and as a result,

the induced field becomes large. This induced field is responsible for the electromagnetic enhancement.

Chemical Enhancement

Another type of field enhancement comes up from chemical enhancement mechanism which comprises of charge-transfer transition between metal and the molecules attached with the metal particles. In this type of enhancement, either (i) the electronic states of the adsorbate are broadened and shifted by their interaction with the surface or (ii) new electronic states that arise from chemisorption serve as resonant intermediate states in the Raman scattering.

However, in this review, we have mostly concentrated on electromagnetic enhancement.

Plasmonic Behavior of Ag and Au

Figure 1a, b illustrates the plot of $Re[\varepsilon(\lambda)]$ and $Im[\varepsilon(\lambda)]$ of dielectric function of bulk flat Ag and Au as a function of wavelength, respectively, in the UV-VIS-NIR region. The real part of dielectric function for both the Ag and Au appears to be similar since they have similar electron densities [29, 30]. But, the imaginary part which is related to the light absorption of the material is very different for those metals at wavelength <600 nm and turn out to be similar above 600 nm. Au shows double-hump structure in the imaginary part below 600 nm which arises from the inter-band electronic transition. However, above 600 nm, the imaginary part of Au and Ag
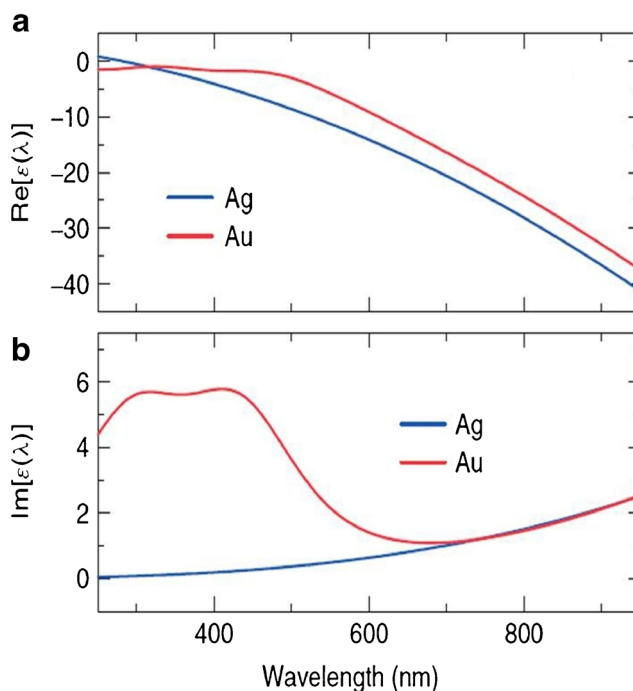

Fig. 1 Plot of dielectric functions of bulk Ag and Au as a function of wavelength: **a** real part and **b** imaginary part [29]

becomes comparable like the real part, indicating both the metals are equally efficient in the specified range. Figure 2a demonstrates the reflectance spectra of bulk Ag and Au in the UV-VIS-NIR region considering complex dielectric function. Ag is highly reflective in the entire visible region of the electromagnetic spectrum, whereas Au shows 50% reflectivity ≤600 nm which are the reason for the whitish and yellowish color of bulk silver and gold, respectively. But, in the long wavelength region (>600 nm), Au reflects as much as Ag which makes it useful for visible/NIR reflector. Another important factor of interest for plasmonic device application is the local field enhancement intensity factor (LFIEF) which is nothing but the ratio of intensity of the electromagnetic field in the presence of metal to the intensity of field in that particular point without metal. LFIEF at any specific point is proportional to the square of electric field intensity, i.e., $|E(r)|^2$ which can be expressed explicitly as follows[29]:

$$\text{LFIEF} = \frac{|E(r)|^2}{|E_o(r)|^2} \tag{7}$$

where $|E_o(r)|$ is the electric field intensity of the incoming ray at that point. Depending on LFIEF >1 or <1, the nomenclature of the optical phenomenon will be "enhancement" or "quenching," respectively. LFIEF on the surface of the Au and Ag interface with air are shown in Fig. 2b. LFIEF is generally <1 at the interface of the flat surface of pure bulk metal separating from air indicating quenching of field intensity at the surface. In the case of ideal lossless flat bulk metal surface, induced electric field on metal surface efficiently cancels out exactly the incoming one and suppresses transmission making the metal a highly reflective surface which guarantees zero LFIEF. Therefore, a low LFIEF for real bulk metal surface may be thought of a natural consequence of high reflectivity. However, real metal surface shows low LFIEF because of the incomplete cancelation of the incoming field. For instance, LFIEF is >1 for Ag when $\lambda \leq 400$ nm where Ag acts as a poor reflector.

Ag and Au are of the best choice for plasmonic device application since they have negative $\text{Re}[\varepsilon(\lambda)]$ ranging from 0 at $\lambda \rightarrow \lambda_p$ to very large at $\lambda \rightarrow \infty$ which makes them promising to satisfy resonance conditions. But, in case of $\text{Im}[\varepsilon(\lambda)]$, both the Ag and Au differ much in the wavelength region below 600 nm indicating higher optical absorption and becoming negligible for both the Ag and Au above 600 nm. LFIEFs for both the Ag and Au spheres have been depicted in Fig. 3 which clearly shows that Ag outperforms over Au in a number of cases. Au is as good as Ag above 600 nm wavelength region as far as the LFIEF is concerned. Although, Ag demonstrates high LFIEF, sharp resonance peak as compared to Au, practical application of SERS is really important in the visible range, especially, above 600 nm, since many biological SERS-based detectors use VIS-NIR lasers. Au is chemically more stable in the long run and bio-compatible with many molecules of interest. Therefore, for biological application, Au would be the most preferred for SERS substrate. Other coinage metals and transition metals including Pt, Pd, Cu, Co, Ni, and their alloys are hardly use for SERS application because of the unsuitable dielectric function. More
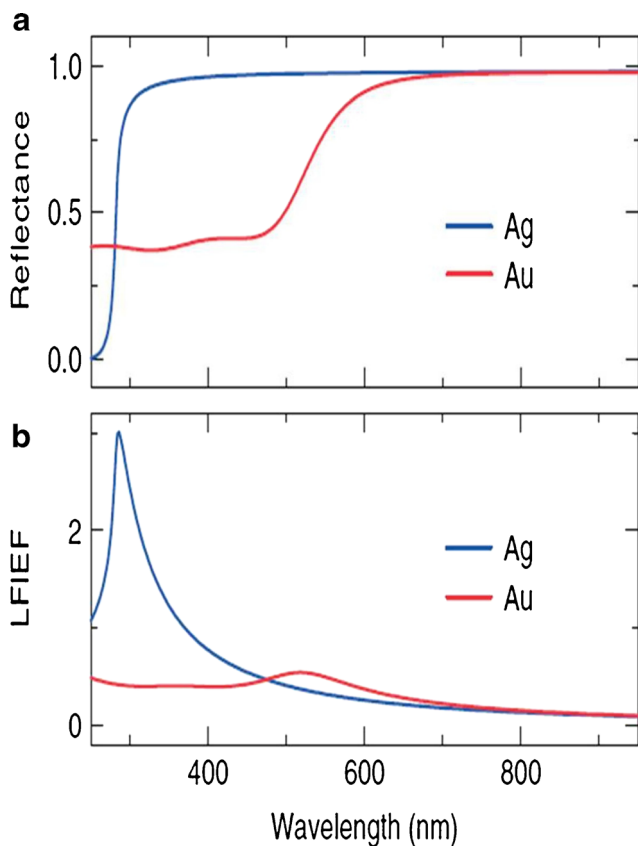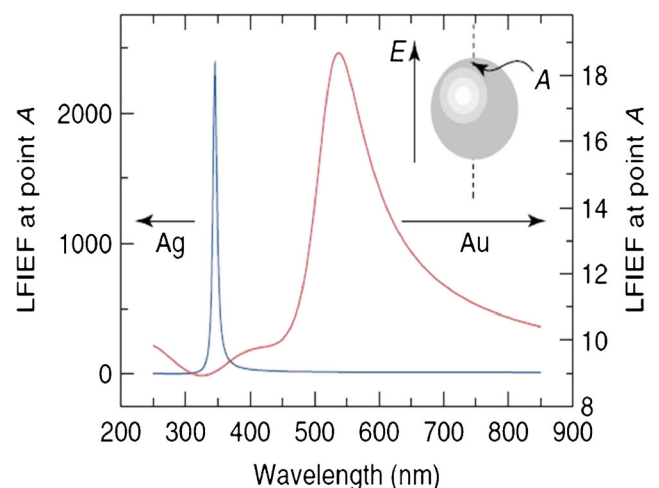

Fig. 2 **a** Reflectance spectra of bulk Ag and Au in the UV-VIS-NIR region and **b** comparison of the LFIEF on the surface of Ag and Au in UV-VIS-NIR region [29]

Fig. 3 LFIEFs for Ag and Au nanospheres [29]

specifically, negative Re[$\varepsilon(\lambda)$] for those materials may satisfy the resonance condition; a large Im[$\varepsilon(\lambda)$] which are at least one order larger than that of Au and Ag limits their plasmonic application. However, they are sometimes studied for academic interest or for some specific applications such as SERS in the UV region.

Size Effect

LFIEF on flat bulk metal surface is not so significant which indicates that bulk metals do not present any major advantages as far as SERS is concerned, except enhancement of reflectivity. The novel photonic properties in metal arise when its size and shape are taken into account [31]. If an object is small (diameter of few nanometers) compared to wavelength of the incident radiation, the problem can be solved electrostatically where it is assumed that electric field of the light in any case becomes approximately constant at all over the object and will look like a uniform field oscillating up and down at a frequency of ω. For wavelengths in the visible range 500–600 nm, the electrostatic approximation is mostly valid for objects of sizes in the range of 10 nm or smaller [29]. Basically, when electromagnetic wave hits the particle, electron cloud is pushed to one side of the particle leaving behind positively charged cores on the opposite side to form a dipole. But, as the direction of incoming oscillatory electric field alters, electron cloud moves in the opposite direction which reverses the direction of the induced dipole. Thus, free electron cloud is driven to oscillation at the same frequency as the incoming light.

Shape Effects

LFIEF is a geometry-dependent function. The simplest geometries like spheres and cylinders associate with single resonance condition whereas features like triangles and cubes may satisfy multiple resonance because of the greater degree of charge separation available in particles with sharp corners. Highly symmetric feature like spheres generally produces single resonance peak; however, a small shoulder peak is sometimes observed owing to the quadrupole resonance (i.e., orientation of two dipoles in opposite directions) caused by the non-uniform incident of light across the sphere [32]. Multiple resonance peaks mainly appear due to the decreased symmetry in the structure [32]. A number of peaks observed can be correlated with the number of ways in which the electron density can be polarized. It is a common tendency for the charges to be concentrated at the sharp corners of low symmetry features which are sometimes referred to as the "lightning rod effect." Superior charge separation reduces the Coulombic restoring force, increasing the time required for each oscillation and lowering the frequency which appears as "red shifting" of resonance peak compared to spherical particles in addition to the appearance of multiple peaks in

the spectrum. For equilateral triangular NP, all vertices are in principle equivalent but the direction of the electric field eventually eliminates the symmetry and causes non-uniform field distribution too which is shown in Fig. 4. However, LFIEF in more complicated shapes can be significantly high and may contain multiple peaks in some circumstances if the shape has sharp corners as compared to the simplest shapes like spheres or cylinders.

Coupled Resonance

When two cylinders or spheres are far apart from each other, the situation can be treated as two different independent problems of single cylinders/spheres. But, when they approach to each other at a closer proximity, the field produced by their respective induced dipoles starts interacting and introduces another important effect in NSs, named "coupled plasmon resonance" which causes a change in the spatial configuration of the fields and reinforces or weakens the field in a certain region of space. When the features are close enough to each other, a clear red shift of the strongest peak (the dipolar interaction coupled plasmon resonance) observes in accordance with a very large field enhancement (LFIEF). The enhancements at the gap between metallic nano-objects are termed as "hot spots" [30] which are shown in Fig. 5. Coupled resonance, however, provides some of the highest field enhancements among the optical spectroscopy available.

Fabrication Techniques

Synthesis of Ag and Au NPs

It is noteworthy to discuss the synthesis of Au and Ag NPs with extremely high control over size, shape, and number density which are imperative from the SERS-based detection point of view. Xie et al. [33] reported medical applications of Au and Ag NPs for SERS-based quantitative detection of micro-organisms, intracellular monitoring of thiopurine
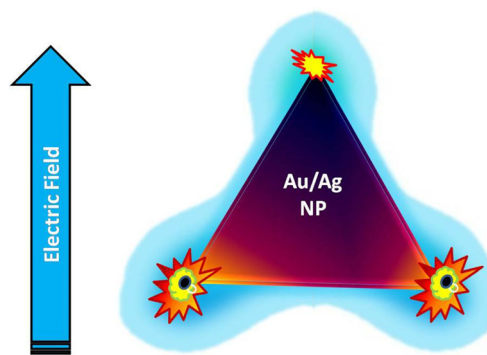

Fig. 4 LFIEF at the vertices of an equilateral triangular noble metal particle
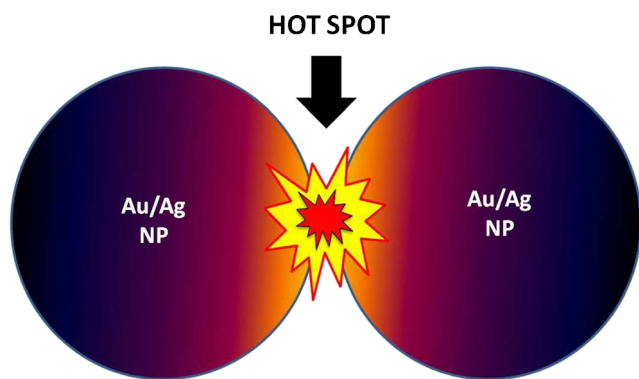
HOT SPOT

Fig. 5 Schematic representation of coupled resonance and corresponding hot spot

anticancer drug release, and detection of the potential pancreatic cancer marker MUC4 antigens in serum. Ren et al. [34] used Ag NP-coated graphene oxide as SERS substrate for the label-free detection of folic acid in water and serum based on the inherent SERS spectra of folic acid. It is also reported that Au NSs can be applied for diagnostics and plasmonic photothermal therapy of cancer, using strongly enhanced surface plasmon resonance absorption of Au NPs and NRs [35]. However, synthesis processes of Ag and Au NPs have already been reported by several research groups following various techniques which have been discussed in the following section.

Ag NP Synthesis

Nanosilver in the form of colloid has been used as bio-medical material since the last hundred years although until very recently, the nomenclature "nano" has been used. Lea et al. [36] first reported synthesis of citrate stabilized Ag colloid with average particle size of ~7–9 nm which is similar to recent reports on nanosilver fabrication using silver nitrate and citrate. A number of techniques including chemical reduction method, electrochemical deposition, and thermal evaporation have been demonstrated so far to synthesize silver NPs. Among them, chemical reduction method has been widely studied, due to its advantages of yielding NPs without aggregation and mass production at low cost. Chemical reduction technique primarily involves the reduction of $AgNO_3$ by a reducing agent in the presence of a suitable stabilizer which protects NPs from aggregation. Preparation of silver colloid by reducing $AgNO_3$ aqueous solution using trisodium citrate ($Na_3C_6H_5O_7$) as reducing agent is quite a well-known process [37, 38]. A yellow-colored colloid generally forms as a consequence of the citrate reduction of $AgNO_3$ to Ag NPs. In a chemical reduction method, particle size and agglomeration state of Ag NPs depend on the precursor concentration, stabilizer concentration, reaction time, temperature, etc. Stable Ag sol was also prepared by Henglein et al. [39] by γ-irradiation of a solution containing $AgClO_4$, N_2O, 2-propanol, and citrate
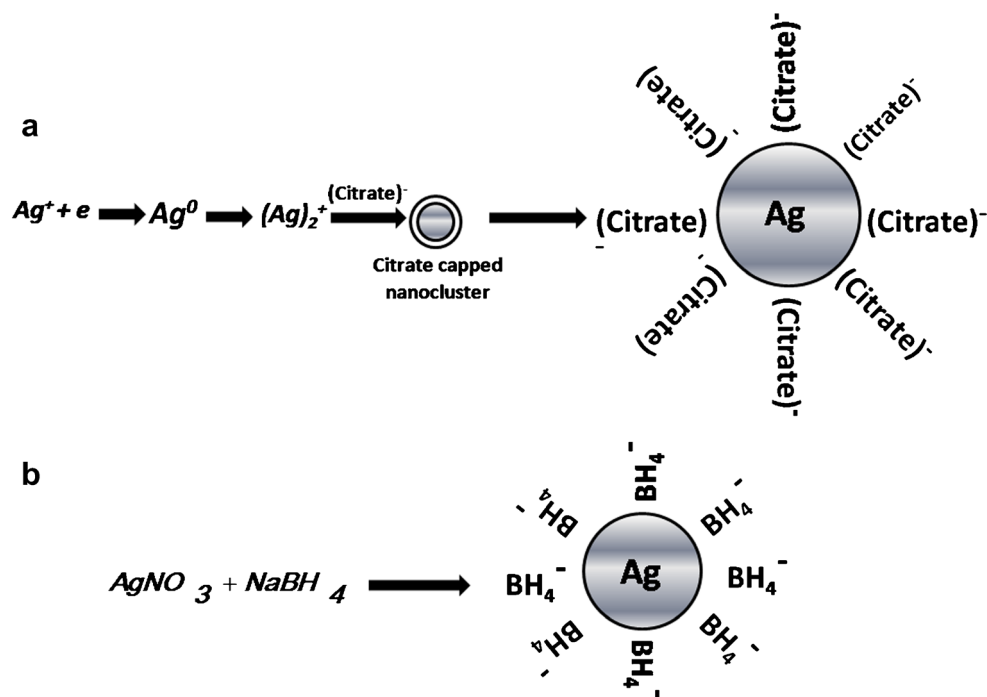
for various concentrations. In this report, the particle size and agglomeration process were observed to be dependent on the citrate concentration which produce agglomerated Ag particles at low precursor concentrations, smaller sized NPs at medium concentration, and large lumps of coalesced NPs at higher concentration. Another well-known strong reducing agent, sodium borohydride ($NaBH_4$), was also exercised for the production of Ag-based yellow colloid by reducing $AgNO_3$ [40]. However, Ag NPs, prepared using $NaBH_4$ as reducing agent, are generally smaller in size compared to the NPs formed in the citrate reduction process. Unlike trisodium citrate, Ag NPs can be prepared from $AgNO_3$ even at room temperature using $NaBH_4$ as a reducing agent because of its extremely high reducing efficiency. Trisodium citrate or $NaBH_4$ not only participate in the reduction process of metal salt but also serve as a stabilizer by surface adsorption of (citrate)$^-$ or BH_4^- ions on the NP surface which prevents the NPs from coalescence owing to the electrostatic repulsion of negatively charged surfaces. Surface adsorption of (citrate)$^-$ and BH_4^- ions on Ag NP surface and stabilization mechanism have been shown schematically in Fig. 6 [37, 40].

The use of stabilizers in addition to citrate or borohydrate has also been reported for better stabilization of the NPs. Sodium dodecyl sulfate (SDS) was used as a stabilizer in addition to the borohydrate for colloidal Ag NP preparation from $AgNO_3$ [41]. In an another study, Ag NP aggregate was synthesized using a solution of cetyltrimethylammonium bromide (CTAB) and $AgNO_3$ in which $NaBH_4$ was added as the reducing agent. This system produces CTAB-capped highly stable Ag NPs with size ~17 nm [42]. Polyvinylpyrrolidone (PVP) and polyethelene glycol (PEG), well-known organic stabilizers, are being used to prevent the NPs from aggregation even for long time [43].

Other well-known reducing agents, apart from trisodium citrate and sodium borohydrate, have been demonstrated for the fabrication of Ag NPs from $AgNO_3$. Song et al. [44] reported the synthesis of spherical Ag NP-based colloid with particle diameter ~10 nm at 40 °C by dissolving $AgNO_3$ in ammonia water with formaldehyde as the reducing agent and PVP as the stabilizing agent. Pal et al. [45] prepared Ag sol with particle size ranging from 15 to 60 nm by photochemically reducing $AgNO_3$ in Triton X-100 (TX-100), i.e., poly(oxyethylene) isooctyl phenyl in ether medium and ascorbic acid solution.

The use of multiple reducing agents simultaneously for the synthesis of Ag NPs with different shapes and sizes has also been reported. In a study, $AgNO_3$ was reduced using citric acid, sodium citrate, L-ascorbic acid, sodium borohydrate, and sodium bis(2-ethylhexyl)sulfosuccinate [46]. Another group reported synthesis of uniform spherical Ag NPs with size ~16 nm by a process in which aqueous solution containing $AgNO_3$ was reduced to produce Ag NPs by sodium linoleate ($C_{18}H_{32}ONa$), linoleic acid ($C_{18}H_{32}O_2$), and ethanol at

Fig. 6 Surface adsorption of **a** citrate and **b** borohydrate ions on Ag NP surface and stabilization mechanism

a

$Ag^+ + e \longrightarrow Ag^0 \longrightarrow (Ag)_2^+ \xrightarrow{(Citrate)^-}$ Citrate capped nanocluster

(Citrate)$^-$ ... Ag ... (Citrate)$^-$

b

$AgNO_3 + NaBH_4 \longrightarrow$ BH$_4^-$ ... Ag ... BH$_4^-$

the temperatures between 80 to 100 °C [47]. Huang et al. [48] synthesized Ag NP-based colloids containing various sizes and shapes (spherical, rod, triangular, etc.) with tunable optical properties which can be adjusted to generate rainbow colors ranging from violet to red with central peak wavelength of absorption ranging from 393 to 738 nm. In that report, colloidal Ag NPs were prepared by reducing $AgNO_3$ salt using sodium citrate and sodium borohydrite and the NPs were stabilized by PVP. The size and shape of the Ag NPs were found to be responsible for the origination of an independent color in the colloid [48, 49].

Unconventional methods for the synthesis of Ag NPs from $AgNO_3$ have also been explored. Saxena et al. [50] synthesized Ag NPs with diameter of ~34 nm by an inexpensive, environmentally friendly extracellular method by reducing $AgNO_3$ using onion (*Allium cepa*) extract. The same group further synthesized Ag NPs in an unconventional and fast method without using harsh chemicals by reducing $AgNO_3$ using *Ficus benghalensis* leaf extract [51]. It was found that these NPs demonstrate efficient antibacterial activity against *Escherichia coli* bacteria. Green synthesis of Ag NPs has also been reported recently by reducing $AgNO_3$ using green leaf extract [52].

Ag NP synthesis methods that have been discussed so far by the reduction of $AgNO_3$ are in the form of colloid. To obtain the array of NPs on wafer surface (e.g., wafer-based SERS-active substrate), dip coating, spin coating, or spray of colloid followed by a thermal annealing is essential. However, Giorgis et al. [53] reported a simple and efficient technique for the synthesis of Ag NPs directly on solid substrate simply by immersing the freshly etched Si wafer into $AgNO_3$ solution followed by an annealing at 500 °C. Dense growth of Ag NPs with diameter ranging from 20 to 200 nm was obtained by decomposition of $AgNO_3$. This is an efficient technique for the fabrication of wafer-based SERS-active substrate. In an another study, closely packed, highly dense (~10^{11}/cm^2), and uniform-sized Ag NPs on semiconductor substrates were fabricated by electrochemical deposition from aqueous $AgNO_3$ using pulsed signal consisting of a long period with a short pulse duration [54]. It was observed that NPs with size ranging from 14 to 37 nm can be obtained by varying the pulse duration and immersion times. Study on the synthesis of NPs by the vapor phase method has also been reported using an inert gas condensation (IGC) process where silver was evaporated under a vacuum in the argon atmosphere, and the particles formed in the gas phase were deposited on a stainless steel flat surface cooled by flowing liquid nitrogen [55]. Particles with a size of 16 nm were collected by brushing them off the stainless steel plate with a Teflon scraper.

Au NP Synthesis

Long before the progress of modern gold chemistry, special manifestation of gold was appreciated by mankind: reddish colloid was exercised to color glasses and ceramics. Colloidal gold were also used in bio-medical applications including tonics and elixirs and to treat arthritis etc. [56]. However, after the famous experiments of Faraday [57] to generate gold colloid in the middle of the nineteenth century, beginning of the chemistry of gold colloid occurred

scientifically. At the beginning of the twentieth century, Oswald [58] made a breakthrough in the colloidal science after which the term "colloidal" has often been substituted by "nanoparticle" or "cluster." Miniaturization of size of Au in the nanometer range consequences modification in physical, electrical, and chemical properties compared to its bulk counterpart which include change in color, lowering of melting point, origination of localized surface plasmon, and alteration of electrical conductivity. Therefore, Au NP synthesis has drawn much attention by a number of routes including chemical reduction of $HAuCl_4$ using trisodium citrate, sodium borohydrate, photocatalytic reduction techniques, thermal evaporation of pure gold metal, etc.

Colloidal Au NPs have been synthesized from aqueous $HAuCl_4$ solution by citrate reduction technique using sodium citrate as the reducing agent [59, 60]. Paul et al. [62] found that the size and morphology of the NPs are dependent on the $HAuCl_4$ to $C_6H_5Na_3O_7$ molar ratio and fine and spherical Au NPs with diameter of ~20 nm were obtained by a conventional citrate reduction technique for the $HAuCl_4$ to $C_6H_5Na_3O_7$ ratio of ~1:3.5. Synthesis of spherical NPs and nanoplatelets of Au by the modified citrate reduction method has also been reported which contains additional ultrasonic irradiation in contrast to the simple citrate reduction technique [62]. It was observed that the particle size reduces and the shape becomes more regular spherical with the increase of ultrasonication time. It was further concluded that ultrasonication is a much more powerful tool to engineer the particle size and shape. Lee et al. [63] also investigated the effect of sonication on the size of Au NPs, produced by the citrate reduction method. It was concluded that $HAuCl_4$ to $C_6H_5Na_3O_7$ molar ratio and the sonication energy affect significantly the size and morphology of the NPs. In another study, Au NPs with uniform diameter was prepared by a facile method comprising of three steps [64]. At first, mixture solution of $HAuCl_4$ and trisodium citrate was made and $NaBH_4$ was added into it under stirring condition. Toluene solution containing 1-nonanethiol was then added into the gold colloid under a vigorous stirring. Finally, the organic phase was separated from the mixture and was refluxed in the toluene solution. In the first step, the particle size obtained was of 3–4 nm which gradually increased in the next steps probably due to aggregation. The group further reported the fabrication of two-dimensional/three-dimensional super lattices of Au NPs by evaporating the solvent from the colloidal solution at optimal concentration [64]. Colloidal Au NPs (spherical) were also prepared from aqueous chlorauric acid ($HAuCl_4.3H_2O$) by citrate reduction using X-ray irradiation [65]. The size of the NPs was found to be dependent on the concentration of the precursors and X-ray irradiation duration. Jimenez et al. [66] studied the effect of solvent isotropic replacement (H for D, i.e., replacement of water by Deuterium oxide) on the size of Au NPs, synthesized by citrate reduction of $HAuCl_4$ using

sodium citrate in heavy water (D_2O). With increasing replacement of H_2O by D_2O, reaction became faster and as a consequence, smaller sized Au NPs were obtained. Therefore, by this process, NPs with controlled size can be fabricated.

Debnath et al. [67] first time reported the synthesis of Au NPs of size ranging from 6.3 ± 2.1 to 27.9 ± 6.2 nm by the solid-state method using $KAuCl_4$ and $NaBH_4$ and PVP at room temperature where $NaBH_4$ was used as a reducing reagent of gold salt and PVP as to protect the particles from agglomeration. The particle size was adjusted by varying the reaction time or by changing the mass average molar mass of the polymer or by changing the mass ratio of the reactants used. Smaller particles were obtained by using long-chain PVP or lower concentration of gold precursor with short-chain PVP. Larger particles were grown by using short-chain PVP with the higher gold precursor concentration.

Au NPs were also prepared by femto second laser ablation of a gold metal plate in aqueous solutions of cyclodextrins (α-CD, β-CD, γ-CD) using a Ti/sapphire laser that gives 110 fs full width at half maxima pulses [68]. The radiation was focused onto a gold rod which was placed on the bottom of a 3-mL glass vessel filled with aqueous solutions of cyclodextrins (α-CD, β-CD, γ-CD). β-CD is most effective in reducing the size and dispersion of the gold NPs. If the ablation was done in pure water, the particle size of 40–50 nm would be obtained which is in contrast with the NP size of ~2.1–2.3 nm (size distribution less than 1 nm FWHM) obtained from laser ablation in 10 mM β-CD. Au NPs were also prepared by the solid-state non-aqueous method by high-speed vibration milling.

Fabrication of Au NPs with multiple shapes has also been reported by varying experimental parameters. Sau et al. [69] reported the preparation of a number of structural architectures including rods, rectangles, hexagons, cubes, triangles, star-like NPs, and branched NSs (e.g., bi-, tri-, tetra-, and multipods) at room temperature in aqueous solution in the presence of a surfactant by systematic varying the experimental parameters. Grzelczak et al. [70] and Alexandridis [71] summarized the recent reports on the controlled growth of Au NPs with multiple sizes and discussed various chemical mechanisms that govern the anisotropic growth.

Fabrication of Vertically Aligned Si NW Array

It is a key challenge to fabricate a vertically aligned NW array with very high aspect ratio and number density on silicon wafer by an inexpensive technique. Silicon NWs assembled or aligned onto a variety of substrates including flexible to transparent substrates using both established and cutting-edge methods have been reported by various techniques such as laser ablation, chemical vapor deposition, metal-catalytic growth, oxide-assisted growth, VLS technique, and MacEtch of Si wafer [72–90]. But, most of these techniques involve high temperature and complex fabrication arrangement that

make the process multifaceted. To our knowledge, MacEtch is the best economic and simple way to grow high aspect ratio, crystalline, dense fabrication of desirable doped, and vertically aligned Si NWs.

MacEtch is basically a wet chemical and directional etching technique which is exercised as an electroless etching using a discontinuous layer of noble metals on Si wafer surface in hydrofluoric acid (HF) and an oxidative agent mixture solution. The technique requires noble metals such as Ag, Au, Pt, and Cu which induce local oxidation and reduction reaction under an open circuit [91–102]. It causes selective removal of semiconductor adjacent to the metal surface and yields NW or porous semiconductor structures. The first manifestation of MacEtch of Si was reported by Dimova et al. [103] where porous Si was fabricated by etching an aluminum (Al)-covered Si substrate in a solution containing a molar ratio of HF/HNO$_3$/H$_2$O = 1:3:5. In this report, incubation time necessary for the formation of porous structure was found to decrease significantly due to the presence of Al film on the Si substrate. Li and Bohn [104] made a thorough study on MacEtch and found that thin layer of noble metal (e.g., Ag, Au, Pt) sputtered on Si substrate acts as a catalyzer during etching of Si in a solution composed of HF, H$_2$O$_2$, and ethanol which results formation of straight pores or columnar structures. In general, etching of Si by MacEtch is performed using HF and H$_2$O$_2$ as etchant [87, 105–108]. The oxidative agent, H$_2$O$_2$, oxidizes Si preferentially adjacent to the noble metal faster and "off-metal areas" slower but the etching rate solely depends on the noble metal morphology, properties of the etchant, electrical properties, and crystallographic orientation of the Si substrate. As a result, columnar structures with diameter of few tens of nanometer form in the regions without metal coverage.

A number of possible cathode and anode reactions have been reported to explain MacEtch [110–111] which are comparable to the anodic etching of Si in HF [112] or stain etching of Si in HF/HNO$_3$ [113, 114]. In case of MacEtch of Si, a discontinuous layer of Ag or Au was used which makes metal-semiconductor contact with Si. Metal not only forms metal-semiconductor junction with Si but also plays a role as a catalyst for the reduction of oxidant. As a consequence of this metal-semiconductor contact and microscopic redox reaction, metal (Ag or Au) acts as a microscopic cathode and withdraws electron from the underlying Si (i.e., injection of hole to Si) through the metal Si junction resulting local oxidation of Si which gets dissolved by HF [87, 116–117] in the subsequent step. Cathode reaction for the reduction of H$_2$O$_2$ and formation of hole can be expressed by the following reactions [104, 118]:

$$H_2O_2 + 2H^+ \rightarrow 2H_2O + 2h^+ \tag{8}$$
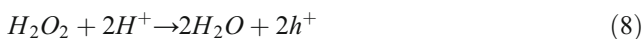
whereas reduction of protons into hydrogen and generation of hole is another well-accepted cathode reaction:

$$2H^+ \rightarrow H_2\uparrow + 2h^+ \tag{9}$$

For chemical etching of p-type Si in a solution containing HF and H$_2$O$_2$, the cathodic current density (j) can be expressed as [119–121]:

$$j = -zek_cn_sC \exp\left(-E_a\Big/KT\right) \tag{10}$$

where z is the number of electrons transferred during the reaction, e is the charge of an electron, k_c is the rate constant, n_s is the electron density, C is the H$_2$O$_2$ concentration, E_a is the activation energy of the reaction, and K is the Boltzmann constant.

At anode, Si substrate gets oxidized and later on dissolves by the following reactions with HF:
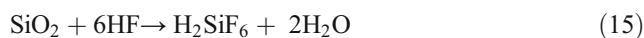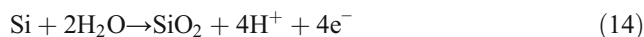
1. If Si dissolution occurs directly in its tetravalent state [122, 123],

$$Si + 4h^+ + 4HF \rightarrow SiF_4 + 4H^+ \tag{11}$$
$$SiF_4 + 2HF \rightarrow H_2SiF_6 \tag{12}$$

2. If there is direct dissolution of Si in its divalent state [124],

$$Si + 4HF_2^- \rightarrow SiF_6^{2-} + 2HF + H_2\uparrow + 2e^- \tag{13}$$
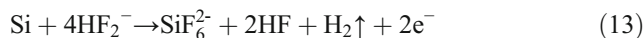
3. If Si oxide formation is followed by dissolution of oxide [125, 126],

$$Si + 2H_2O \rightarrow SiO_2 + 4H^+ + 4e^- \tag{14}$$
$$SiO_2 + 6HF \rightarrow H_2SiF_6 + 2H_2O \tag{15}$$

As an end result, metal-semiconductor junction is continuously mentioned which enables incessant movement of the etching front. Thus, the part of the Si wafer attached with noble metal in general gets etched by hole diffusion and subsequent dissolution method by HF and etching front goes down producing an up and down structure on the Si wafer surface due to the presence of the discontinuous metal layer [127, 128]. MacEtch mechanism for Si by hole diffusion process has been shown schematically in Fig. 7. The overall etching process can be summarized as (i) reduction of oxidant at the surface of the noble metal due to the catalytic activity, (ii) hole diffusion through metal-semiconductor interface and injection into Si, (iii) oxidation of Si and dissolution of oxide by HF, and (iv) hole diffusion from the Si, under the noble metal

Fig. 7 MacEtch mechanism of Si in H_2O_2/HF solution following hole diffusion process. (*i*) Reduction of oxidant at the surface of the noble metal due to the catalytic activity. (*ii*) Hole diffusion through metal-semiconductor interface and injection into Si. (*iii*) Oxidation of Si and dissolution of oxide by HF. (*iv*) Hole diffusion from the Si, under the noble metal to the off-metal areas
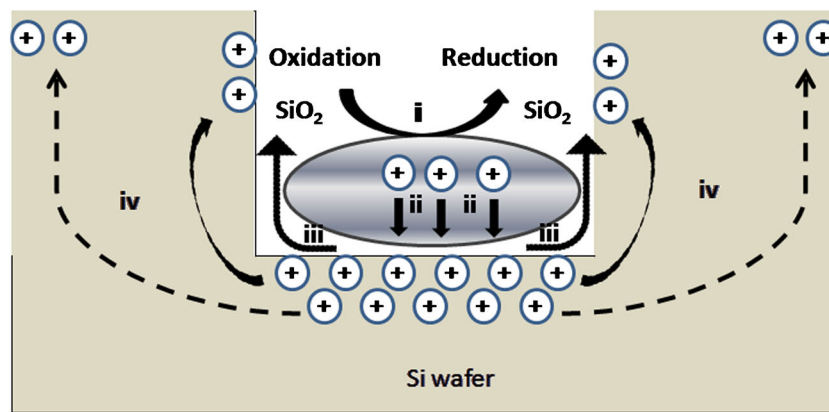
to the off-metal areas. However, the etching rate depends on concentrations of HF and H_2O_2, temperature, and crystallographic orientation of Si wafer [129, 130]. Charge transfer is indispensable for the oxidation and dissolution of Si by the MacEtch method. Hole injection is well accepted as a charge-transfer process for electroless etching of Si. Since the generation of holes is directly related to the decomposition of H_2O_2 on the metal surface, the amount of holes that can be injected into Si will increase with the increase of H_2O_2 concentration (*C*). Concentration of holes further depends on the reaction temperature because of the temperature-dependent decomposition rate of H_2O_2 [129]. At low temperature, catalytic decomposition rate of H_2O_2 becomes limited and hence lower cathodic current. At higher temperature, as expected, the decomposition rate of H_2O_2 increases which in turn increases hole density and cathodic current as well. However, H_2O_2 is the best choice among the available oxidants, viz., HNO_3 [130, 131], $KMnO_4$ [132], $Fe(NO_3)_3$ [133, 134], $K_2Cr_2O_7$ [132], etc., that are generally used in stain etching of Si because of the much more positive electrochemical potential as compared to the valance band of Si and other oxidants as well.

It is further well accepted that wet chemical etching of Si in most of the inorganic etchant (e.g., KOH) is anisotropic which occurs at different rates in different crystallographic directions [135]. Etching of Si (100) is faster compared to Si (111) planes because of the less numbers of Si back bonds (two for each atom) in contrast to Si (111) where three bonds need to break to remove an Si atom. Si (110) shows the fastest etching followed by (100) and (111).

Another MacEtch method for the fabrication of Si NWs, using $AgNO_3$, mixed with HF as oxidant in lieu of H_2O_2 has also been reported [137–138]. A galvanic cell forms when Si is immersed in $AgNO_3$/HF solution since the electrochemical potential of Ag^+/Ag is more positive than the Fermi energy of Si [137, 139]. As a consequence, hole inject into the valance band of Si takes place from Ag^+ which then gets reduced to elemental Ag. These self-formed Ag particles participate in chemical etching of Si by the following reactions [137]:

$$Ag^+ + e^- \rightarrow Ag \tag{16}$$

$$Si + 6F^- \rightarrow SiF_6^{2-} + 4e^- \tag{17}$$

This technique does not require an additional discontinuous noble metal layer for the etching to carry out but reduced Ag particle deposit on Si surface and form micro-/nanocathodes which oxidize Si and subsequent dissolution of oxide layer occurs underneath the Ag particles by HF, maintaining continuous Ag/Si interface. Thus, Ag particles sink inside Si and nanowires are formed between the particles having diameter similar to the inter-Ag particle distance. Various steps for metal-assisted chemical etching of Si wafer in $AgNO_3$/HF solution have been depicted schematically in Fig. 8a–d. Tree-like dendritic growth of silver is generally found on the top of the Si NWs after completion of the MacEtch process [138] which can be removed to get Si NW arrays by dissolving the dendrites in (1:1 *v/v*) HNO_3/H_2O at room temperature. SEM image of the silver dendrite structure formed in the MacEtch technique is shown in Fig. 8e, f. MacEtch of Si wafer using $AgNO_3$, mixed with HF, is inexpensive and useful for the fabrication of vertical arrays of Si NWs with diameters as small as 5 nm to as large as 1 μm. The technique enables to have control over some properties of the yields which include length, crystallographic orientation, and doping level.

Synthesis of aligned Si NWs by vapor methods has also been reported. Kayes et al. [140] and Hochbaum et al. [72] reported the fabrication of vertically aligned Si NW array by VLS mechanism using noble metal catalyst (Cu, Au, etc.). Highly crystalline, dense Si NW array with controlled diameter can be achieved in this technique. But, catalyst droplets appear either at the top or at the base of the NWs after completion of the growth which usually act as impurity and
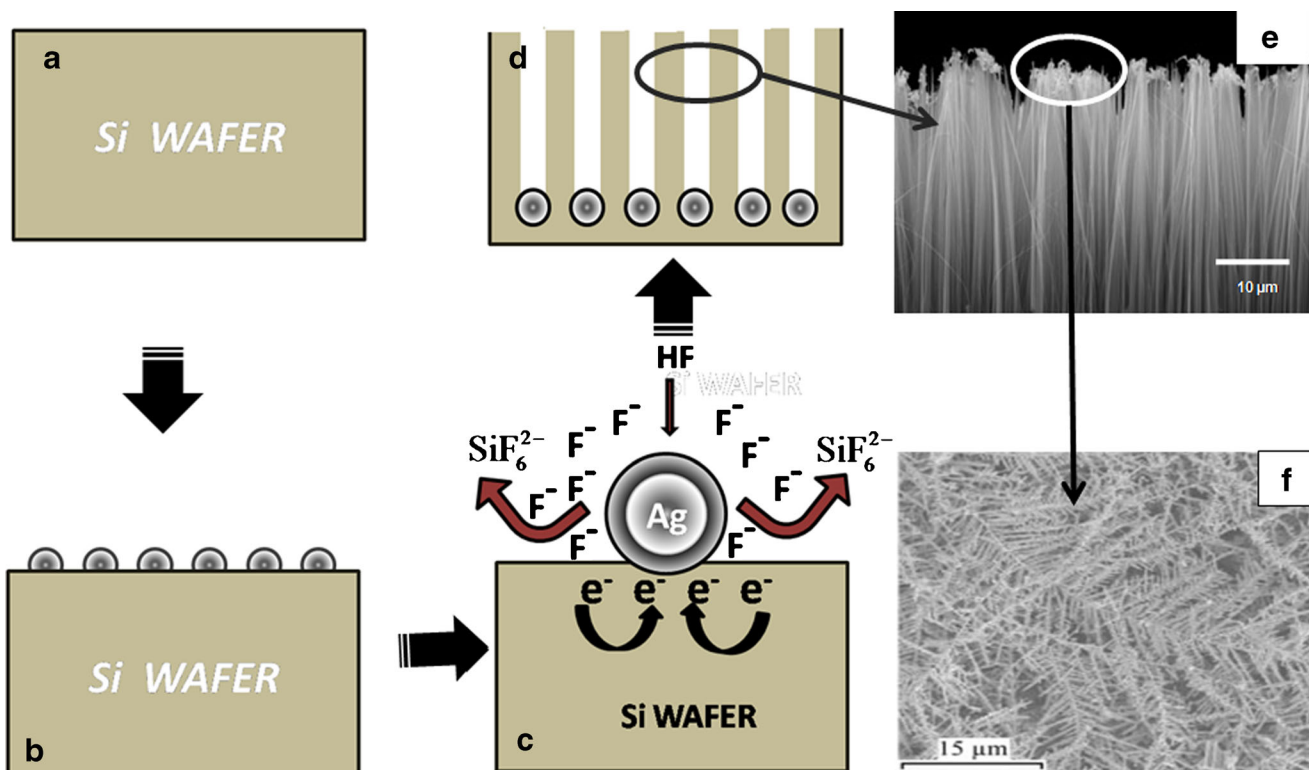
Fig. 8 Various steps of MacEtch of Si in AgNO₃/HF solution have been shown schematically. **a** Clean Si wafer. **b** Self-formation of Ag NPs on Si surface from the reduction of AgNO₃. **c** Formation of Ag/Si nanogalvanic cell where Ag NP acts as cathode and Si as anode. Reaction at cathode and corresponding etching mechanism. D Vertical array of formed Si NWs. **e** Cross-sectional SEM image of Si NWs fabricated by MacEtch technique with silver dendrites on the top. **f** SEM image of silver dendrite at higher magnification [138]

deteriorate electrical and other properties of the semiconductor NWs. Post-fabrication chemical etching is a mandate to remove those impurities. SEM image of the copper-catalyzed Si NW array with Cu droplets on the top of the NWs has been shown in Fig. 9. However, high temperature, hazardous silicon precursors, complex instrumentation, and rigorous experimental conditions limit its application for low-cost device fabrications. Therefore, the template-based MacEtch technique has widely been exercised for the controlled synthesis of vertical array of Si NWs at low temperature and simple and inexpensive technique as compared to the VLS method.

Template-Based Synthesis of Si NW Array

Above discussions seem that MacEtch of Si is quite impressive for the fabrication of dense, vertically aligned Si NW array by inexpensive technique. MacEtch of Si wafer in AgNO₃/HF solution produces vertically aligned Si NW array but the technique does not provide much flexibility to play over the diameter and density of the NWs owing to self and random deposition of Ag particles. On the other hand, in the MacEtch technique, using pre-deposited discontinuous noble metal layer on Si in H₂O₂/HF solution, diameter and density of the NWs can be controlled by the dimension and density of

the discontinuity in the metal film. In the following section, we have mostly concentrated on the controlled fabrication of vertically aligned Si NW array by the MacEtch method.

An approach has been made by Huang et al. [141] to fabricate vertically aligned Si NW array with different diameters and sizes by utilizing very high pore density and periodicity of anodic aluminum oxide (AAO) membrane. The group reported the synthesis of well ordered, vertically aligned array of Si NWs with diameter ranging from 8 to 20 nm and number density as high as 10^{10}/cm² using ultrathin AAO membrane as mask. Surface pre-patterning of Si substrate followed by MacEtch can efficiently yield vertical array of Si NWs. In surface patterning process, an ultrathin AAO membrane/ polystyrene composite was placed on a cleaned Si surface. A subsequent reactive ion etching (RIE) was performed under SiF₆/O₂ plasma to pattern Si of the uncovered region. A thin film of Ag or Au was then deposited on patterned Si substrate by sputtering which took part in etching of Si in the succeeding step by the MacEtch method using HF/H₂O₂ mixture. Deposition of Ag causes a continuous film on the flat part of the Si surface with particles at the bottom of the pores which occurs owing to the surface pre-patterning of the Si wafer. No Ag deposition, however, was found at the side wall of the pores. It was further observed that the rate of chemical
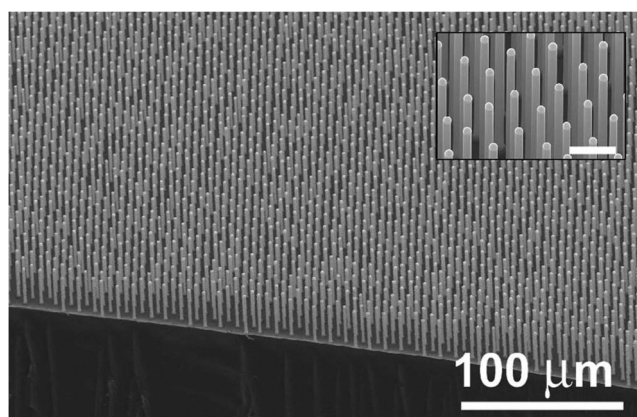
Fig. 9 FESEM image of VLS grown Si NW array using CU catalyst. *Inset* shows magnified FESEM image of the NWs with catalyst droplets on the tips [140]

etching by Ag film is much faster than that of the Ag particles and, as a consequence [141], Ag NPs were found on top of the NWs which are shown schematically in Fig. 10. As mentioned in the "Fabrication of Vertically Aligned Si NW Array" section, catalyst particles are generally found on the tip or at the base of the NWs after completion of growth by VLS mechanism; here also, a similar trend was observed in the form of Ag NPs on the tip of the NWs although the synthesis technique (MacEtch) is completely different from VLS. Difference in the etching rate for both the Ag film and Ag NPs in MacEtch method results formation of array of axially aligned Si NWs on Si substrate. It was further observed that the diameter and number density of the NWs depend on the pore diameter, thickness of the metal film and pore density of the AAO mask, since the metal mess exactly takes the shape of the underlying AAO mask. However, upon close investigation of the NW synthesized by Huang et al. [141], it was viewed that the NWs have smooth surfaces and have tapered morphology with different diameters at the top and bottom. According to this report [141], dissolution of Ag during etching by the etching solution consequences gradual increase of the pore size of the Ag film and diameter of the resulting Si NWs increase accordingly. Kim et al. [142] also observed the dissolution of Ag layer using MacEtch in etching solution. As a remedy, patterned bilayer nanopore meshes of Au/Ag were exercised for the MacEtch of Si. Since Au is inert against oxidative dissolution in etching solution (i.e., HF and H_2O_2), the Au layer on the upper side of Au/Ag bilayered metal mesh efficiently prevents the undesired structural disintegration of the underlying Ag layer and tapering of the Si NWs as well, acting as a catalyst for H_2O_2 decomposition on its surface. Bilayered structure was fabricated by depositing 5 nm of Au film on 15 nm of Ag film by sequential sputtering on an AAO membrane. Au-/Ag-coated AAO membrane was then floated on the surface of NaOH etchant solution to dissolve the underlying AAO membrane and detach the bilayer mesh from AAO. Then the bilayer mesh was floated

on a dilute nitric acid solution to remove the loose metal NPs from the bottom side of the bilayered structure, and the resulting metal mesh was transferred onto a Si wafer and dried. Fabrication of bilayered metal mesh and transferring method onto Si substrate have been shown schematically in Fig. 11. Finally, bilayered metal mesh-loaded Si wafers were etched by the MacEtch technique in the H_2O_2/HF solution to fabricate vertically aligned Si NW arrays. SEM images shown in Fig. 12a illustrate spatial arrangement of the NWs with uniform diameters along their axis and smooth side walls which have arrangement similar to the pore array in the bilayered metal mesh. However, bilayered metal mesh was found at the bottom of the NWs after completion of the etching process (Fig. 12b). In an another study, the group further reported the synthesis of straight and well-defined zigzag cross-sections of Si NWs imposing vertical gradient of etchant concentrations during chemical etching by varying HF/H_2O_2 molar ratio [143]. In this study, they used very thin (~30 nm) gold mesh as catalyst which was fabricated by depositing Au thin film on AAO surface followed by a chemical etching of AAO membrane. The transfer technique of Au mesh onto the Si wafer surface was similar to the transfer technique of bilayered metal film exercised in previous report [142]. Fabrication of ultrathin, straight Si [111] NWs with uniform ribbon-like structure and curved Si NWs with controlled turning angles by using MacEtch method at elevated temperature have also been demonstrated. According to Kim et al. [143], zigzag NWs formed by a two-step MacEtch method where the first step etching was performed by immersing the Au mesh-loaded Si wafer in 2.424 M HF in 10.572 M H_2O_2 solution (HF/H_2O_2 = 0.229) for 10 min followed by dipping into 46 wt% HF solution for 10 s. The resulting structure was spaghetti-like porous Si, covering contentiously throughout the mesh surface. This sample was further immersed into etchant solution composed of 24.242 M HF and 1.057 M H_2O_2 (HF/H_2O_2 = 22.935) and the resulting zigzag Si NW structure was formed. It was reported that in direct chemical etching of Si (100) wafer at room temperature in the absent of the first step (i.e., spaghetti-like porous Si surface formation), etching would produce straight NWs, irrespective of HF/H_2O_2 molar ratio. However, HF/H_2O_2 ratio influences the morphology of the NWs without affecting their axial direction. When HF/H_2O_2 is >1.2, porous Si NWs form. A porous continuous thin film occurs when HF/H_2O_2 is <1.2. Fabrication of zigzag NWs is very interesting and noteworthy from the application point of view owing to the very large exposed surface area. TEM image of zigzag NWs is shown in Fig. 13. Initially, a straight NW down to several micrometers was formed which changed shape to zigzag by changing axial orientation of straight arm that altered between two specific crystallographic directions. The dimension of the zigzag NWs at the two different points (straight arm (w_1) and turning points (w_2)) differ by $w_1 < w_2$. Mechanism for the formation of zigzag

Fig. 10 Schematic of the fabrication process of ordered Si NW array. **a** Surface pre-patterned Si substrate. **b** MacEtch to form NW array with Ag NPs on the tips [141]
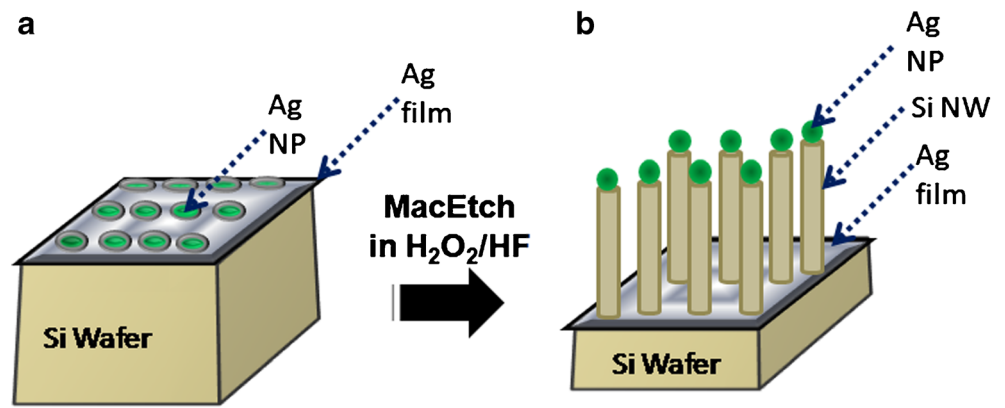
NWs in the MacEtch technique can be explained by the hole diffusion model. For etchant solution with high relative H_2O_2 concentration (e.g., $HF/H_2O_2 < 1.2$), generation of holes increases (Eq. 10) and removal of oxidized Si will be slowed down because of the unavailability of sufficient HF to cause etching. As a result, extra amount of holes that are not consumed by oxidative dissolution of Si can diffuse away from etching front to the off-metal areas or side walls of the pores resulting in vertically porous NW array or spaghetti-like Si after the first step of the MacEtch technique. Formation of zigzag NWs is governed by the diffusion-controlled chemical etching method. Spaghetti-like porous Si surface plays a dominant role by regulating diffusion of the reactants and creating a vertical gradient of etchant concentration on the reaction interface as well. In the second step of chemical etching, higher HF concentration was used as compared to H_2O_2 ($HF/H_2O_2 = 22.935$) which causes fast depletion of H_2O_2 near the etching front, resulting a sharp concentration gradient of H_2O_2 along the direction perpendicular to the reaction

interface. Depletion of H_2O_2 at the reaction front will cause retardation of cathodic current (j) which is directly proportion to the H_2O_2 concentration at low temperature. Thus, hole injection into Si will be limited which remain localized at the Si (100) plane with the fewest Si back bonds to break, resulting in a one-dimensional etching along <100> direction. Within a very short time, H_2O_2 concentration gets resumed by vertical diffusion of etchant and j increases further. As a consequence, switching of the etching direction occurs from <100> to slanted non-<100> directions. After consumption of the diffused etchant at the etching front, depletion of H_2O_2 takes place again, making it a cyclic process which in turn results periodic oscillation of cathodic current (j). With this oscillation of current, growth direction of NWs switches between <100> to non-<100> directions with the periodicity determined by the concentration gradient of H_2O_2 between bulk etchant reservoir and the etching front and diffusivity of the etchant. Therefore, oscillating cathodic current (j) seems to be a sinusoidal function of time which leads to form zigzag NWs

Fig. 11 Schematic of Si NW fabrication process. **a** AAO membrane. **b** Bilatered mesh of Au/Ag on AAO membrane. **c** Removal of AAO by 1 M NaOH solution. **d** Cleaning and transferring of bilayered mesh on Si substrate [142]
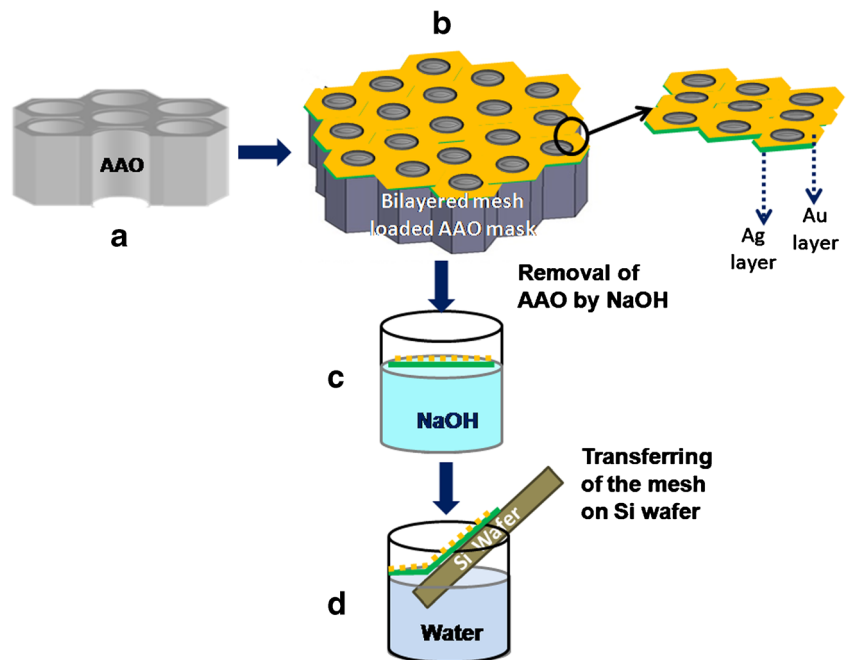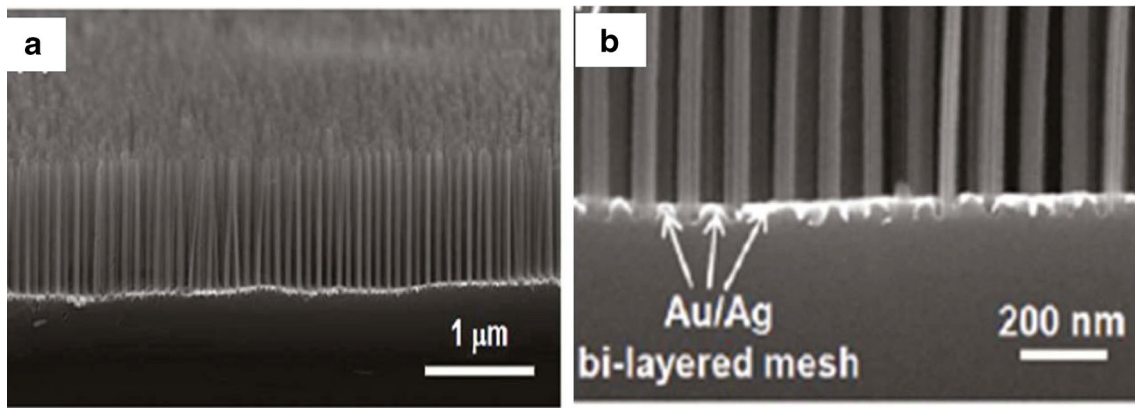
Fig. 12 a Cross-sectional FESEM image of the Si NW array grown by using bilayered metal mesh [142]. **b** Magnified FESEM image which shows clearly the Si NW array with bilayered metal mesh at the bottom [142]

with tunable arm length and turning angle (θ). However, etching temperature also affects etching direction which turns out to be faster at higher temperature and yields tilted ultrathin aligned NWs [142].

Huang et al. [144] reported the synthesis of vertically aligned Si NWs with controlled diameter, length, and density using self-assembly of polystyrene (PS) sphere array as a mask followed by thermal deposition of Ag film and
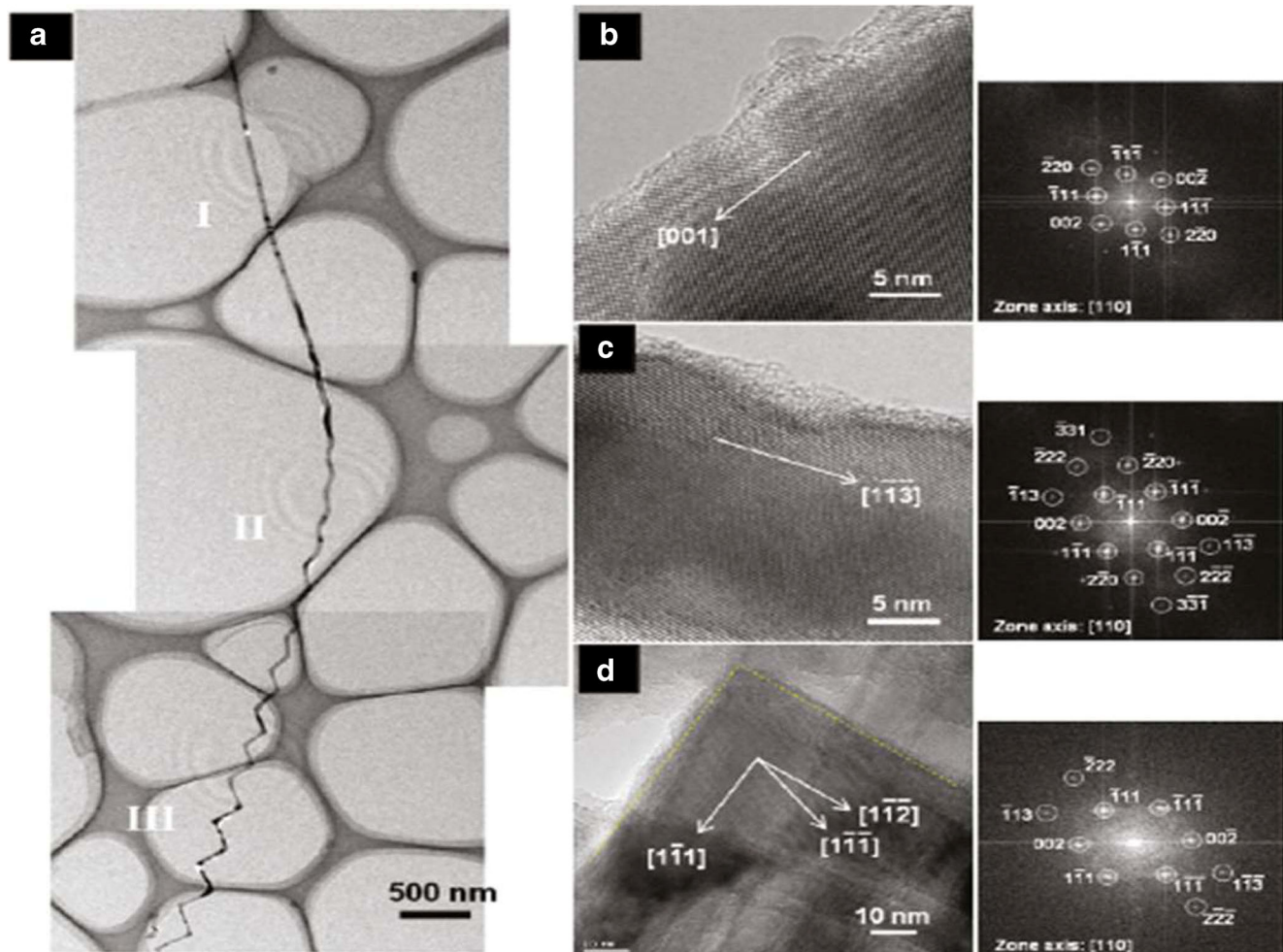

Fig. 13 (a) TEM images of a single zigzag Si NW by MacEtch of Si (100) substrate [143]. Nanowire parts formed during the early, middle, and last stage of the second-step chemical etching are marked by *I*, *II*, and *III*, respectively. **b–d** High resolution TEM images from the NW parts corresponding to *I*, *II*, and *III*, respectively, and corresponding FFT patterns are displayed on the *right side* of the respective panels

MacEtch technique. Monolayer of PS spheres with diameter of 260 and 360 nm were used as a mask whose diameter can be reduced to a desired value by varying the duration of RIE. MacEtch was performed in a 4.6 M H_2O_2 and 0.44 M HF mixture solution. Schematic representation of the Si NW fabrication process using PS spheres has been depicted in Fig. 14. After the MacEtch process, PS was removed from the top of the NWs by immersing the samples into $CHCl_3$ solution, and finally, Ag film was removed by immersion in boiled aqua regia. A large area array of vertically aligned Si NWs with diameter ranging from 50 nm to several microns was formed in this technique. The diameter of the NWs depends on the diameter of the PS spheres used. In order to obtain Si NWs with diameters less than 20 nm, the mask must be made by reducing the diameter of PS spheres using RIE but this process leads to the formation of Si NWs with irregular cross-sectional geometry.

Another efficient way to fabricate ordered and densely packed arrays of high-aspect-ratio Si NWs is the block-copolymer lithography method. Chang et al. [145] coated Si substrate with 60-nm-thick SiO_2 by e-beam evaporation. Diblock copolymer, polystyrene-block-ployferrocenyldimethylsilane (PS-b-PFS), was then spin coated on the SiO_2/Si substrate followed by vacuum annealing. The PS matrix was subsequently removed by oxygen plasma,

leaving behind well array PFS dots on SiO_2/Si surface. Unmasked SiO_2 layer was then etched by RIE to form pillar structures of SiO_2 with the PFS dots at top and Au film was subsequently deposited on the sample by e-beam evaporation. Finally, SiO_2 pillars were etched by HF solution which left pores of diameter equal to the diameter of the PFS dots, leaving behind an Au mesh on the Si substrate. Finally, vertically aligned Si NW array was fabricated by MacEtch of this Au mesh-loaded patterned Si wafer in H_2O_2 and HF solution. Figure 15 demonstrates schematically the fabrication process of the Si NWs using diblock copolymer. Vertical arrays of NWs with aspect ratio of ~220, diameter below 20 nm, and spacing of 10 nm were achieved in this technique.

Choi et al. [146] fabricated perfectly periodic Si NWs and nanofin arrays over large area Si substrate by a new type of approach which is a combination of interference lithography (IL) and catalytic etching. At first, Si substrates with thick layer of photoresist were exposed in a Lloyd's mirror type IL setup with a HeCd laser source of wavelength (λ) ~325 nm and then unexposed photoresist was removed using Microposit MF CD-26 developer which left circular photoresist dot pattern on the wafer surface. Subsequent oxygen plasma etching was employed to remove the residual unexposed photoresist and to reduce the size of the photoresist dots. Au thin film of thickness ~25 nm was deposited on the patterned
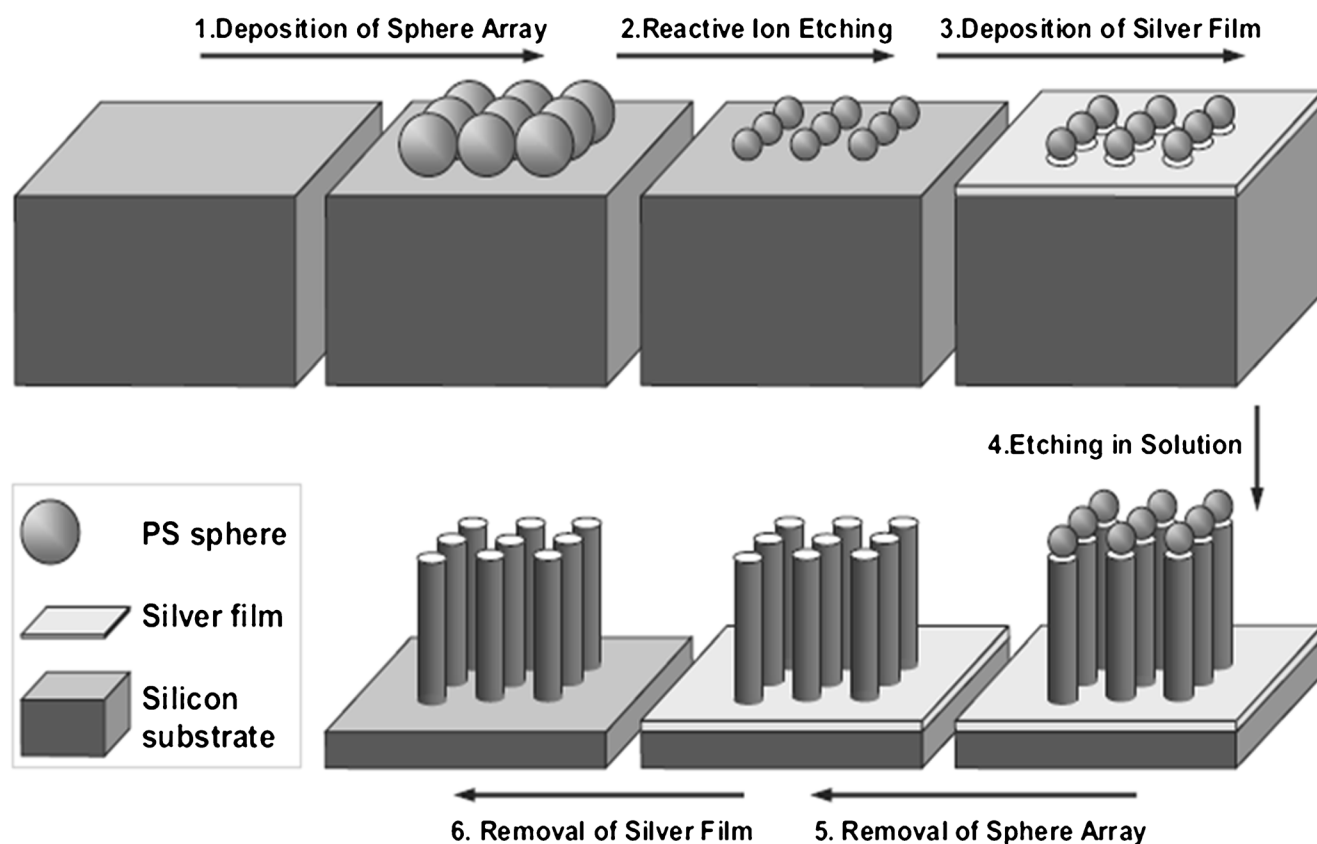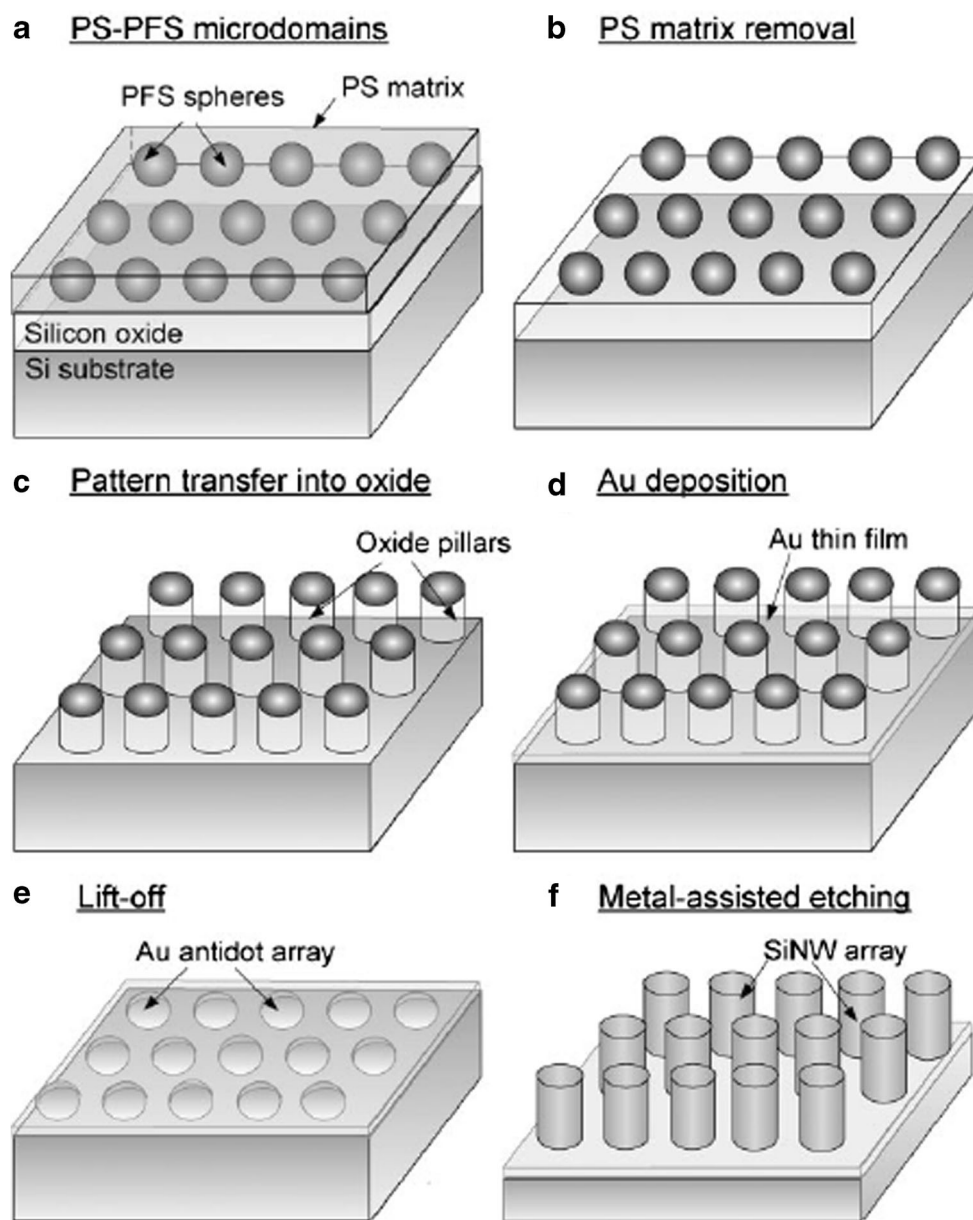

Fig. 14 Schematic representation of the Si NW fabrication process in a method combining nanosphere lithography and MacEtch process [144]

a PS-PFS microdomains

PFS spheres — PS matrix

Silicon oxide
Si substrate

b PS matrix removal

c Pattern transfer into oxide

Oxide pillars

d Au deposition

Au thin film

e Lift-off

Au antidot array

f Metal-assisted etching

SiNW array

substrate by thermal evaporation. Finally, Au-coated patterned samples were etched by MacEtch in a solution containing HF and H_2O_2 at room temperature. After completion of etching, Au and photoresist layers were dissolved in proper etchant. Schematic for the Si NW fabrication steps by IL method is depicted in Fig. 16a–e. Perfect NW arrays with well-defined orientation, diameter, length, and number density (Fig. 16f) were obtained in this technique.

Fabrication of SERS Substrate

Field enhancement in SERS using noble metal NPs can efficiently be used for the detection of bio-molecules up to the single molecular limit. Among the large number of SERS-

related reports, all the currently used SERS substrates can be categorized into five broad classes depending on the underlying fabrication method: (i) colloidal metal nanostructures, (ii) metal NPs assembled on flat substrates, (iii) metal NPs assembled on one-dimensional nanostructures, (iv) regular metal nanolithographic nanostructures, and (v) "SERS tags."

Colloidal Ag or Au suspension is easy to synthesize and inexpensive and provides sufficient SERS enhancement. Premasiri et al. [147] reported the quantitative detection of individual components of human urine such as, urea, uric acid, creatinine, and albumin by SERS method using colloidal Au solution. Quantitative SERS analysis of human urine was also investigated which indicates the possibility of using SERS as a replacement of present pathological detection method and commercialization of Raman spectroscopy. This is a highly
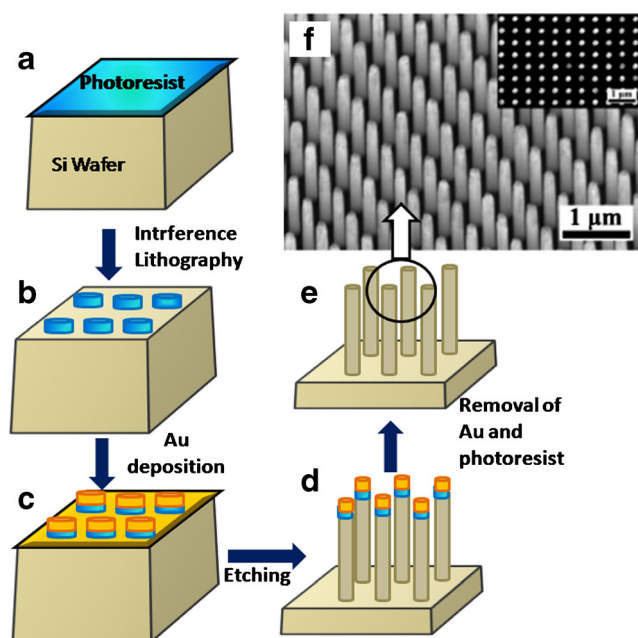
Fig. 16 **a**–**e** Schematic representations of various steps for the fabrication of Si NW array using a combination of interference lithography and MacEtch and (**f**) SEM image of the Si NW array fabricated by this technique. *Inset* shows top view of the NW array [146]

sensitive and fast technique for pathological application but further attention has been paid in order to increase the sensitivity of this technique further by which portable Raman can be used in pathological application to reduce the examination cost. Colloidal Au NPs with average diameter of ~30 nm have also been used by Li et al. [148] for the detection of protein-protein interaction by SERS. But, sensitivity of colloid-based SERS detection is restricted by the limited number density of the noble metal NPs in the colloid and absence of "coupled resonance," i.e., "electromagnetic hot spots" owing to the dispersion of particles in the liquid medium. Recently, Fazio et al. [149] reported detection of bio-molecules like amino acids and proteins, namely phenylalanine, bovine serum albumin, and lysozyme, up to the detection limits in the micrograms per milliliter range using dispersed gold nanorods into the solution of bio-molecules. In the study, it was argued that enhancement of Raman scattering of the bio-molecules occurred at the "hot spots" of the SERS-active clusters which are formed on chemically driven aggregation of metal nanorods in the presence of the target molecules. But, practical application needs specially engineered SERS substrates that provide good tunability, high stability, high sensitivity, reproducibility, and low cost. Major challenges for the real-time detection of bio-molecules are bio-compatibility and high sensitivity. Therefore, tremendous efforts have been paid in order to improve the sensitivity of the SERS substrate for its application in sensor devices. As an antidote, wafer-based SERS substrates made of flat surfaces, patterned by Ag or Au NPs, have been thought of promising for bio-detection because of

mainly the "coupled resonance" and adequate hot spots which provide higher LFIEF ($\sim 10^{12}$) than those of individual particles, in addition to their bio-compatibility [150–161]. Jiang et al. [152] reported the detection of multiplex DNA by Si-based active and reproducible SERS substrate. This Si wafer-based sensor exhibits very high sensitivity with a detection limit down to 1 pM. SERS substrate, made of Au-coated Si wafer, has been used by Liu et al. [153] to detect melamine and its analogue (cyanuric acid), nitrogen rich compounds, up to 2 ppm in liquid milk. This approach leads SERS to detect food contaminants such as melamine in foods and food ingredients very fast with ultrahigh accuracy.

Although, flat SERS-active substrates, made of patterned noble metal film/NPs on wafer surface, are potential devices for the detection of organic/biological molecules, sensitivity of the device can further be enhanced by increasing the active surface area, i.e., by increasing the number density of the NPs. One of the key challenges to increase the surface area of the SERS-active substrate further by which sensitivity of the sensor device can be enhanced is to introduce 1D nanomaterial-based SERS substrates where large exposed surface area of the nanostructures provide enough space to accommodate large number of NPs. Morphology and alignment of the NSs are also important factors to have large effective active surface area and hence the sensitivity of the nanostructure-based sensor devices. Vertically aligned NSs coated with Ag or Au NPs are promising for such applications and are being used in SERS-active sensor devices. Vertically arrayed 1D NSs provide larger surface area compared to other configurations with the same diameter, and the spaces between neighboring 1D NSs encourage the diffusion of analyte throughout the surface of the NSs and enhance the performance of the sensor devices. Bronstrup et al. [162] reported enhanced light absorption efficiency of Si NWs compared to bulk/thin films because of the enhanced absorption cross-section which is much bigger than its geometrical area of the individual NWs. As a consequence, Si NWs with diameters on the order of the wavelength of visible light show strong resonant field enhancement of the incident light. Therefore, Si NWs decorated with Au or Ag NP-based SERS substrates have received much importance for the fabrication of highly sensitive SERS-active substrates. Yin et al. [163] reported direct fabrication of Ag NP-decorated Si NW arrays via an electroless etching method for the detection of enzyme-free hydrogen peroxide. In this study, Si NW arrays were prepared by MacEtch of p-type Si (111) wafer. At first cleaned Si wafers were immersed into an etching solution containing 4.8 M HF and 0.005 M AgNO$_3$ for 1 min to precipitate Ag particle, and the resulting samples were then immediately transferred in another etching solution containing 4.8 M HF and 0.3 M H$_2$O$_2$ at 323 K to undergo MacEtch for 60 min. The samples were then treated with dilute HNO$_3$ (1:1, *v/v*) for 1 h to remove the residual Ag catalyst, and the native oxide layer was removed by subsequent etching using HF.

Finally, Ag NPs were decorated on Si NW arrays by reducing AgNO₃ using H-terminated Si NWs which was obtained during the oxide removal step by HF. Resulting Ag NP-decorated Si NW array-based sensor possesses fast amperometric sensing up to low detection limit, and wide linear response range as well as high sensitivity to H_2O_2. Wang et al. [164] also followed a similar method for the fabrication of Ag NP-decorated Si NW-based SERS substrate for the detection of carbaryl which is an important nitrogen-based pesticide. The resulting SERS-active substrate exhibited superior detection sensitivity of $\sim10^{-17}$ M for Rodamine 6G with linear relationship between the logarithmic intensities and the concentrations. The device was highly reproducible too. Luong et al. [165] reported the detection of malachite green molecules by Ag NP-coated Si NW array-based SERS-active substrates. Si NW array with wire diameter of ~100–200 nm and length of ~13 μm was prepared by Ag-assisted chemical etching of Si (100) wafers followed by chemical dissolution of silver dendrites and native oxide layers by (1:1, v/v) diluted HNO₃ and 5 wt% HF, respectively . To attach the Ag NPs with diameter of ~20–40 nm onto the NW surface, H-terminated (Si-H) NWs were further immersed in AgNO₃ solution to reduce Ag^+ to Ag. TEM image of the Ag NP-coated Si NW is depicted in Fig. 17. SERS-active substrates made in this technique are excellent candidate for malachite green molecule sensing with very high stability, reproducibility, and sensitivity down to $\sim10^{-7}$/mol. He et al. [166] reported very high enhancement factor of $\sim10^{10}$ for DNA detection using Ag NP-coated Si NW-based SERS substrates. Si NWs were synthesized for this study by oxide-assisted growth via thermal evaporation of silicon monoxide powder followed by a chemical etching of oxide layer using 0.1 M NaOH solution, and Ag NPs were attached onto the Si surface by in situ reduction

of AgNO₃ solution by NaOH etched Si NWs. The lowest concentration of DNA ever reported (~1 fM) via SERS was achieved in this technique. A new and facile method was proposed by Zhang et al. [167] for the fabrication of ultrasensitive, stable, and reproducible SERS substrates for the application in bio-molecular sensors. SERS-active substrates were prepared by fabricating Si NW arrays via wet chemical etching of Si wafer as proposed by Peng et al. [168] which was then used as a template for the preparation of SERS-active silver-coated NW arrays. First, Si wafer was etched to form Si NW array in an aqueous HF solution containing Ag^+ ions by seed-induced excessive local oxidation and dissolution of Si wafer. Unlike direct adsorption of Au NPs on Si NW surface by dip coating, Au NPs were attached on NW surface by using a polymer-based functional layer to have a dense and ordered pattern. Si NW surface was modified by using (3-aminopropyl)trimethoxysilane (APTMS) and dried in air. APTMS-modified silicon NWs were then dipped into Au colloid for 8 h in order to immobilize the small gold NPs on the surface of the NWs. Finally, the resulting Au-decorated Si NW arrays were immersed in a plating solution to deposit a thin Ag layer on the NW surface. Schematic representation for the fabrication process of Ag-coated Si NW arrays is shown in Fig. 18. These SERS-active substrates exhibit grand potential for ultrasensitive molecular sensing in terms of high enhancement factor, fast detection, good stability, and reproducibility. It was observed that morphology of Si NW array and the type of the Ag plating solution are the two key factors for determining the signal enhancement factor and sensitivity of detection. Recently, patterned SERS substrates are being used for the detection of bio-species with very high accuracy and repeatability. Yi et al. [169] developed vertically aligned Si NWs with controllable orientation within micro-sized features
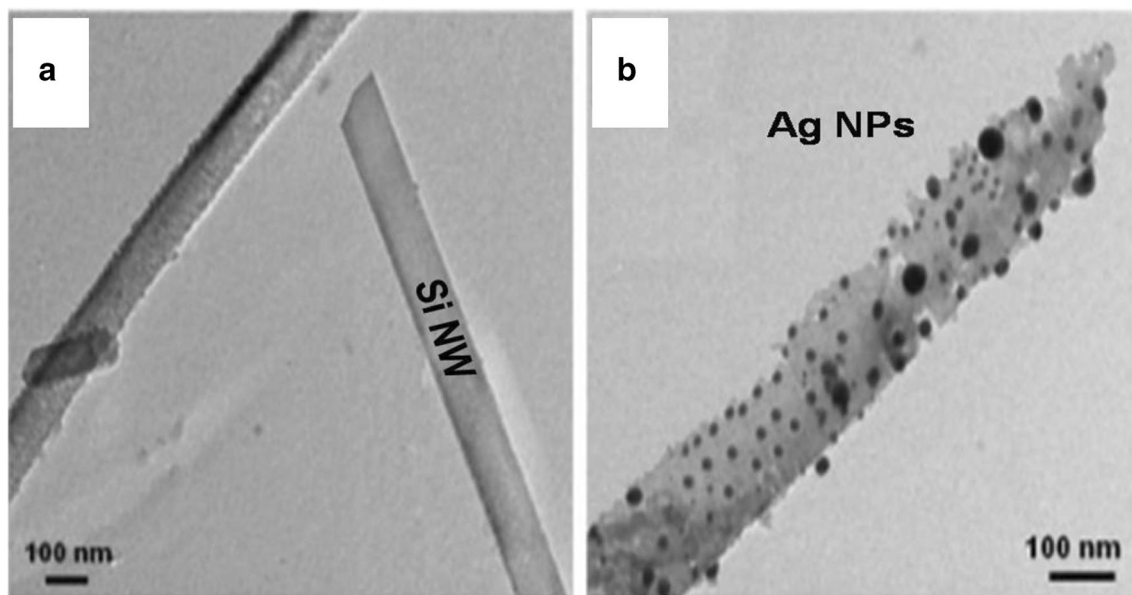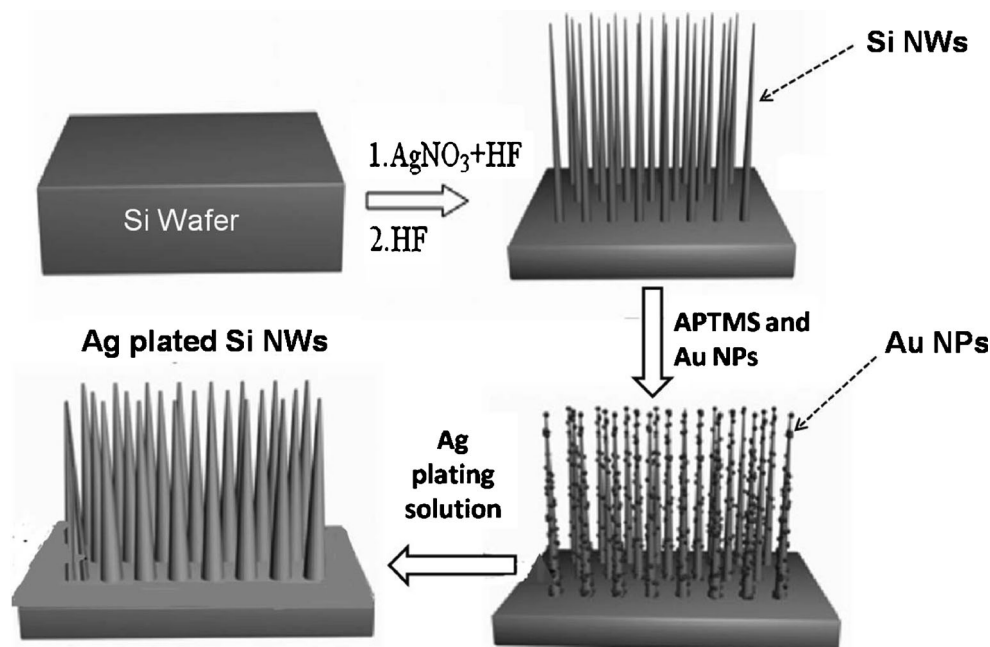

Fig. 17 TEM images of **a** Si NWs grown by MacEtch process and **b** Ag NP-coated Si NW [165]

by single-step photolithography and Ag NP-induced chemical etching at room temperature. These NW-based sensor devices produce a platform for level-free DNA detection using SERS with miniaturized size. DNA molecules were detected efficiently below the concentration of $\sim 10^{-15}$ M using this patterned substrate which can further be applied to tissue engineering. In a report, Wang et al. [170] investigated single-molecule detection on a single Si NW-based SERS sensor, fabricated by controlled deposition of Ag NPs on a Si NW. In this study, Si NWs were synthesized through thermal evaporation of SiO with Sn as a catalyst. SERS sensor was fabricated by controllably depositing Ag NPs on Si NWs and dispersing HF-treated (5%, v/v) Si NWs in cetyltrimethyl ammonium bromide (CTAB) solution followed by metalization in an AgNO$_3$ solution. Single-molecule, real-time detection of Rhodamine 6G was performed on a single Ag NP-coated Si NW SERS sensor in the aqueous phase. This is very important and a breakthrough yet in this field of study.

Summary and Conclusions

Silver and gold exhibit negative real part and negligible imaginary part of dielectric function in the wavelength above 600 nm which satisfies plasmonic resonance conditions making the materials potential for plasmonic device applications. Although, Ag outperforms over Au from the plasmonic point of view because of higher LFIEF, sharp resonance peak, and low optical absorption, Au is chemically more stable in the long run and bio-compatible with many molecules of interest and shows plasmonic vibration in the visible region which makes it promising for biological SERS-based detector applications using VIS-NIR lasers. Alignment of the plasmonic NPs is another factor that governs LFIEF the most. For instance, coupled resonance provides some of the highest field enhancements among the optical spectroscopy available.

Among the large number of synthesis techniques of Ag and Au NPs, chemical reduction of metal salts has been widely studied due to its advantages of yielding NPs without aggression, mass production at low cost. Among the chemical reduction processes, Na$_3$C$_6$H$_5$O$_7$ and NaBH$_4$ have widely been used as reducing agents for Ag or Au NP synthesis from AgNO$_3$ or HAuCl$_4$ compounds, respectively. Unlike trisodium citrate, smaller sized Ag NPs can be prepared from AgNO$_3$ at room temperature using NaBH$_4$, although the reaction is vigorous for the latter case which provides difficulties in control over particle size. Trisodium citrate or NaBH$_4$ not only participates in the reduction process of metal salt but also serve as a stabilizer by surface adsorption of (citrate)$^-$ or BH$_4^-$ ions at the NP surface which prevents the NPs from aggregation. Other polymer-based stabilizers like PVP, CTAB have also been demonstrated to prevent NPs efficiently from aggregation. It is also observed that MacEtch is an economic and simple technique to fabricate vertically aligned high aspect ratio, crystalline, and dense array of Si NWs. MacEtch is performed by electroless etching of discontinuous metal film (Ag or Au)-loaded Si wafer in H$_2$O$_2$ and HF solution. MacEtch of Si wafer in AgNO$_3$/HF solution also produces vertically aligned Si NW array, but the technique does not provide much flexibility to play over the diameter and density of the NWs owing to self and random deposition of Ag particles. On the other hand, in the MacEtch technique, using pre-deposited discontinuous noble metal layer on Si, diameter, and density of the NWs can be controlled by the dimension and density of

the discontinuity in the metal film. The template-based MacEtch technique using AAO, PS, or some other masks which participate in patterning the noble metal film is another potential technique for the fabrication of well ordered, vertically aligned Si nanowire array with controlled diameters and sizes.

Major challenges for the real-time detection of biomolecules are high sensitivity and bio-compatibility. Biomolecular detection by the SERS method using colloidal NPs, NPs on flat wafer surface, and NPs attached to the surface of NWs as SERS-active substrates has been demonstrated. But, sensitivity of colloid-based SERS detectors is restricted by the limited number density of the noble metal NPs in the colloid and absence of "coupled resonance." As an antidote, wafer-based SERS-active substrates made of flat surfaces have been thought of promising for bio-detection because of mainly the "coupled resonance" and adequate hot spots which provide higher LFIEF than those of individual NP. But, number density of the noble metal NPs in the wafer-based SERS-active substrate is limited by the flat area of the wafer. Since the sensitivity of the SERS-based sensor device is proposition-al to the number density of the NPs, it can be enhanced further by introducing 1D nanomaterial-based SERS-active substrates where large exposed surface area of nanostructures provides enough space to accommodate large number of NPs. Si NWs decorated with Au or Ag NP-based SERS substrates have received much importance for the fabrication of highly sensitive SERS-active substrates because of the strong resonant field enhancement caused by the enhanced light absorption cross-section when the diameter of the NWs approaches on the order of the wavelength of visible light. A wide range of analytes like glucose, food components, nicotine, pesticides, DNA, RNA, blood components, urine components, and virus can be detected efficiently by using Si NWs decorated with Au or Ag NP-based SERS-active substrates with very high accuracy even up to the single molecular limit.

Major Challenges

As proposed in this review, fabrication of highly sensitive SERS substrate requires a dense vertically aligned Si NW array and fine and spherical Ag or Au NPs which need to be assembled on the surface of the NWs. Fabrication of freestanding vertically aligned NWs with very high density is really challenging. MacEtch of Si wafer in AgNO$_3$/HF solution yields vertically aligned Si NW array, but the technique does not provide much flexibility to play with the diameter and density of the NWs. In the template-based MacEtch technique, a patterned noble metal film prepared by using AAO and PS as mask produces well-ordered, vertically aligned Si nanowire array with controlled diameter and sizes, but number density of the NWs in this case is limited by the pore density

of the template. However, a big challenge in the MacEtch technique for the fabrication of free-standing vertically aligned Si NW array is the bundling tendency of the NWs during the drying stage due to capillary force caused by the evaporation of water which brings a large number of NW closure to form bundle structure. Bundling of Si NW restricts efficient attachment of NPs on the individual NW surface uniformly. Therefore, a critical drying of the NWs in liquid carbon dioxide can be exercised instead of normal drying in air in order to avoid bundling tendency.

Since SERS is an efficient tool for the detection of a wide range of adsorbate molecules down to the single molecular limit, it can be used in forensic sciences and pathological laboratories as a highly reliable and sensitive detector. However, for commercial applications, the SERS substrate should be stable, reproducible, bio-compatible, and economically viable. Both the Si and Ag/Au are chemically stable and bio-compatible, but from the reproducibility point of view, the alignment of Ag or Au NPs on Si NW surface should be uniform throughout the substrate to get uniform response from any part of the substrate. From the economical point of view, MacEtch of Si and alignment of NPs by using functional layer are viable, but in terms of uniformity throughout the wafer surface, it is really challenging. Therefore, further research needs to be undertaken in these regards for the commercial application of SERS in medical, chemical, biological, and forensic laboratories.

References

1. Jorgenson RC, Yee SS (1993) A fiber-optic chemical sensor based on surface Plasmon resonance. Sens Actuator B 12:213–220
2. Huber A, Demartis S, Neri D (1999) The use of biosensor technology for the engineering of antibodies and enzymes. J Mol Recognit 12:198–216
3. Weiss MN, Srivastava R, Groger H, Lo P, Luo SF (1995) A theoretical investigation of environmental monitoring using surface plasmon resonance waveguide sensors. Sens Actuator A 51:211–217
4. Shankaran DR, Gobi KV, Miura N (2007) Recent advancements in surface plasmon resonance immunosensors for detection of small molecules of biomedical, food and environmental interest. Sens Actuator B. 121:158–177
5. Huang X, El-Sayed IH, Qian W, El-Sayed MA (2006) Cancer cell imaging and photothermal therapy in the near-infrared region by using gold nanorods. J Am Chem Soc 128:2115–2120
6. Barhoumi A, Zhang D, Tam F, Halas NJ (2008) Surface-enhanced Raman spectroscopy of DNA. J Am Chem Soc 130:5523–5529
7. Qian K, Yang L, Li Z, Liu J (2013) A new-type dynamic SERS method for ultrasensitive detection. J Raman Spectrosc 44:21–28

8. Zhang L (2013) Self-assembly Ag nanoparticle monolayer film as SERS substrate for pesticide detection. Appl Surf Sci 270:292–294

9. Jung J, Choo J, Kim DJ, Lee S (2006) Quantitative determination of nicotine in a PDMS microfluidic channel using surface enhanced Raman spectroscopy. Bull Kor Chem Soc 27:277–280

10. Marnian-Lopez MB, Poppi R (2013) Standard addition method applied to the unary quantification of nicotine in the presence of cotinine and anabasine using surface enhanced Raman spectroscopy and multivariate curve resolution. Anal Chim Acta 760:53–59

11. Zhang XF, Zou MQ, Qi XH, Liu F, Zhu XH, Zhao BH (2010) Detection of melamine in liquid milk using surface enhanced Raman scattering spectroscopy. J Raman Spectrosc 41:1655–1660

12. Yonjon CR, Haynes CL, Zhang X, Walsh JT Jr, Van Duyne RP (2004) A glucose biosensor based on surface-enhanced Raman scattering: improved partition layer, temporal stability, reversibility, and resistance to serum protein interference. Anal Chem 76:78–85

13. Neng J, Harpster MH, Wilson WC, Johnson PA (2013) Surface-enhanced Raman scattering (SERS) detection of multiple viral antigens using magnetic capture of SERS active nanoparticles. Biosens Bioelectron 41:316–321

14. Wang TL, Chiang HK, Lu HH, Peng FY (2005) Semi-quantitative surface enhanced Raman scattering spectroscopic creatinine measurement in human urine samples. Opt Quant Electron 37:1415–1422

15. Stiufiuc R, Iacovita C, Lucaciu CM, Stiufiuc G, Dutu A, Braescu C, Leopold N (2013) SERS-active silver colloids prepared by reduction of silver nitrate with short-chain polyethylene glycol. Nanoscale Res Lett 8:47–51

16. Paciotti GF, Myer L, Weinreich D, Pavel D, McLaughlin RE, Tamarkin L (2004) Colloidal gold: a novel nanoparticle vector for tumor directed drug delivery. Drug Deliv 11:169–183

17. Herrera GM, Padilla AC, Hernandez-Rivera SP (2013) Surface enhanced Raman scattering (SERS) studies of gold and silver nanoparticles prepared by laser ablation. Nano 3:158–172

18. Lin D, Feng S, Pan J, Chen Y, Lin J, Chen G, Xie S, Zeng H, Chen R (2011) Colorectal cancer detection by gold nanoparticle based surface-enhanced Raman spectroscopy of blood serum and statistical analysis. Opt Express 19:13565–13577

19. Bhui DK, Bar H, Sarkar P, Sahoo GP, De SP, Misra A (2009) Synthesis and UV-VIS spectroscopic study of silver nanoparticles in aqueous SDS solution. J Mol Liq 145:33–37

20. Desai R, Mankad V, Gupta SK, Jha PK (2012) Size distribution of silver nanoparticles: UV-visible spectroscopic assessment. Nanosci Nanotechnol Lett 4:30–34

21. Haiss W, Thanh NTK, Aveyard J, Fernig DG (2007) Determination of size and concentration of gold nanoparticles from UV-VIS spectra. Anal Chem 79:4215–4221

22. Martinez JC, Chequer NA, Gonzalez JL, Cordova T (2012) Alternative methodology for gold nanoparticles diameter characterization using PCA technique and UV-VIS spectroscopy. Nanosci Nanotechnol 2:184–189

23. Shanmukh S, Jones L, Driskell J, Zhao Y, Dluhy R, Tripp RA (2006) Rapid and sensitive detection of respiratory virus molecular signatures using a silver nanorod array SERS substrate. Nano Lett 6:2630–2636

24. Huang J, Ma D, Chen F, Bai M, Xu K, Zhao Y (2015) Ag nanoparticles decorated cactus-like Ag dendrites/Si nanoneedles as highly efficient 3D surface-enhanced Raman scattering substrates toward sensitive sensing. Anal Chem 87:10527–10534

25. Tabakman SM, Chen Z, Casalongue HS, Wang H, Dai H (2011) A new approach to solution-phase gold seeding for SERS substrate. Small 7:499–505

26. Kosovic M, Balarin M, Ivanda M, Derec V, Marcius M, Ristic M, Gamulin O (2015) Porous silicon covered with silver nanoparticles as surface-enhanced Raman scattering (SERS) substrate for ultra-low concentration detection. Appl Spectrosc 69:1417–1424

27. Alexander KD, Skinner K, Zhang S, Wei H, Lopez R (2010) Tunable SERS in gold nanorod dimers through strain control on an elastomeric substrate. Nano Lett 10:4488–4493

28. Qi H, Glembocki OJ, Prokes SM (2012) Plasmonic properties of vertically aligned nanowire arrays. J Nanomater 2012:1–7

29. Etchegoin PG, Le Ru EC (2011) Surface enhanced Raman spectroscopy: biophysical and life science applications. Ed. Schlucker S Wiley-VCH, Weinheim

30. Kneipp K, Moskovits M, Kneipp H (2006) Surface-enhanced Raman scattering. In: Schatz, G. C.; Young, M. A.; R. P. Van Duyne, R. P (eds) Electromagnetic mechanism of SERS, Spinger-Verlag, Berlin, Vol. 103, , pp 19–46

31. Barnes WL, Dereux A, Ebbesen TW (2003) Surface plasmon subwavelength optics. Nature 424:824–830

32. Cobley CM, Skrabalak SE, Campbell DJ, Xia Y (2009) Shape-controlled synthesis of silver nanoparticles for plasmonic and sensing applications. Plasmonics 4:171–179

33. Xie W, Schlucker S (2013) Medical applications of surface-enhanced Raman scattering. Phys Chem Chem Phys 15:5329–5344

34. Ren W, Fang Y, Wang E (2011) A binary functional substrate for enrichment and ultrasensitive SERS spectroscopic detection of folic acid using grapheme oxide/Ag nanoparticle hybride. ACS Nano 5:6425–6433

35. Huang X, Jain PK, Et-Sayed IH, Ei-Sayed MA (2007) Gold nanoparticles: interesting optical properties and recent applications in cancer diagnostics and therapy. Nanomedicine 2:681–693

36. Lea MC (1889) On allotropic forms of silver. Am J Sci 37:476–491

37. Pillai ZS, Kamat PV (2004) What factor control the size and shape of silver nanoparticles in the citrate ion reduction method? J Phys Chem B 108:945–951

38. Bastus NG, Merkoci F, Piella J, Puntes V (2014) Synthesis of highly monodisperse citrate-stabilized silver nanoparticles of up to 200 nm: kinetic control and catalytic properties. Chem Mater 26:2836–2846

39. Henglein A, Giersig M (1999) Formation of colloidal silver nanoparticles: capping action of citrate. J Phys Chem B 103:9533–9539

40. Solomon SD, Bahadory M, Jeyarajasingam AV, Rutkowsky SA, Mulfinger C (2007) Synthesis and study of silver nanoparticles. J Chem Edu 84:322–325

41. Song KC, Lee SM, Park TS, Lee BS (2009) Preparation of colloidal silver nanoparticles by chemical reduction method. Korean J Chem Engg 26:153–155

42. Sun, L.; Song, Y.; Wang, L.; Guo, C.; Sun, Y.; Liu, Z.; Li, Z. Ethanol-induced formation of silver nanoparticle aggregates for highly active SERS substrates and application in DNA detection. J Phys Chem C 2008, 112, 1415–1422.

43. Tejamaya M, Romer I, Merrifield RC, Lead JR (2012) Stability of citrate, PVP, and PEG coated silver nanoparticles in ecotoxicology media. Environ Sci Technol 46:7011–7017

44. Song HY, Ko KK, Oh IH, Lee BT (2006) Fabrication of silver nanopartiles and their antimicrobial mechanism. Eur Cell Mater 11:58

45. Pal A, Pal T (1999) Silver nanoparticle aggregate formation by a photochemical method and its application to SERS analysis. J Raman Spectrosc 30:199–204

46. Jiang XC, Chen WM, Chen CY, Xiong SX, Yu AB (2011) Role of temperature in the growth of silver nanoparticles through a synergetic reduction approach. Nanoscale Res Lett 6:1–9

47. Das R, Nath SS, Chakdar D, Gope G, Bhattacharjee R Preparation of silver nanoparticles and their characterization. J Nanotech Online. doi:10.2240/azojono0129

48. Huang T, Xiao-Hong NX (2010) Synthesis and characterization of tunable rainbow colored colloidal silver nanoparticles using single-nanoparticle plasmonic microscopy and spectroscopy. J Mater Chem 20:9867–9876

49. Haes AJ, Van Duyne RP (2004) A unified view of propagating and localized surface Plasmon resonance biosensors. Anal Bioanal Chem 379:920–930

50. Saxena A, Tripathi RM, Singh RP (2010) Biological synthesis of silver nanoparticles by using onion (*Allium cepa*) extract and their antibacterial activity. Digest J Nanomater Biostr 5:427–432

51. Saxena A, Tripathi RM, Zafar F, Singh P (2012) Green synthesis of silver nanoparticles using aqueous solution of *Ficus benghalensis* leaf extract and characterization of their antibacterial activities. Mater Lett 67:91–94

52. Johnson I, Joy Prabhu H (2015) Green synthesis and characterization of silver nanoparticles by leaf extracts of *Cycas circinalis*, Ficus amplissima, *Commelina benghalensis* and *Lippia nodiflora*. Int Nano Lett 5:43–51

53. Giorgis F, Descrovi E, Chiodoni A, Froner E, Scarpa M, Venturello A, Geobaldo F (2008) Porous silicon as efficient surface enhanced Raman scattering (SERS) substrate. Appl Surf Sci 254:7494–7497

54. Chen F, Jiang H, Kiefer AM, Clausen AM, Ting Y-H, Wendt AE, Ding B, Lagally MG (2011) Fabrication of ultrahigh-density nanowires by electrochemical nanolithography. Nanoscale Res Lett 6(444):1–7

55. Raffi M, Hussain F, Bhatti TM, Akhter JI, Hameed A, Hasan MM (2008) Antibacterial characterization of silver nanoparticles against *E. coli* ATCC-15224. J Mater Sci Technol 24:192–196

56. Schmid G, Corain B (2003) Nanoparticlculated gold: synthesis, structures, electronics and reactivities. Eur J Inorg Chem 2003: 3031–3098

57. Faraday M (1857) The bakerian lecture: experimental relations of gold (and other metals) to light. Phil Trans R Soc A 147:145–181

58. Ostwald C-Z (1907) 1, 291

59. Bastus NG, Comenge J, Puntes V (2011) Kinetically controlled seeded growth synthesis of citrate-stabilized gold nanoparticles of up to 200 nm: size focusing versus Ostwald ripening. Langmuir 27:11098–11105

60. Khan AK, Rashid R, Murtaza G, Zahra A (2014) Gold nanoparticles: synthesis and applications in drug delivery. Trop J Pharma Res 13:1169–1177

61. Yang J, Tan X, Shih W-C, Cheng MM-C (2014) A sandwich substrate for ultrasensitive and label-free SERS spectroscopic detection of folic acid/methotrexate. Biomed Microdevices. 16:673–679

62. Chen H-J, Wen D (2011) Ultrasonic-aided fabrication of gold nanofluids. Nanoscale Res Lett 6(198):1–8

63. Lee J-H, Choi SUS, Jang SP, Lee SY (2012) Production of aqueous spherical gold nanoparticles using conventional ultrasonic bath. Nanoscale Res Lett 7(420):1–7

64. Xu Z-C, Shen C-M, Yang T-Z, Zhang H-R, Li H-L, Li J-Q, Gao H-J (2005) From aqueous to organic: a step-by-step strategy for shape evolution of gold nanoparticles. Chem Phys Lett 415:342–345

65. Long NN, Vu LV, Kiem CD, Doanh SC, Nguyet CT, Hang PT, Thien ND, Quynh LM (2009) Synthesis and optical properties of colloidal gold nanoparticles. J Phys Conf Series 187:1–8

66. Ojea-Jimenez I, Romero FM, Bastus NG, Puntes V (2010) Small gold nanoparticles synthesized with sodium citrate and water: insights into the reaction mecganism. J Phys Chem C 114:1800–1804

67. Debnath D, Kim SH, Geckeler KE (2009) The first solid-phase route to fabricate and size-tune gold nanoparticles at room temperature. J Mater Sci 19:8810–8816

68. Kabashin AV, Meunier M, Kingston C, Luong JHT (2003) Fabrication and characterization of gold nanoparticles by femtosecond laser ablation in an aqueous solution of cyclodextrins. J Phys Chem B 107:4527–4531

69. Sau TK, Murphy CJ (2004) Room temperature, high-yield synthesis of multiple shapes of gold nanoparticles in aqueous solution. J Am Chem Soc 126:8648–8649

70. Grzelczak M, Perez-Juste J, Mulvaney P, Liz-Marzan LM (2008) Shape control in gold nanoparticle synthesis. Chem Soc Rev 37: 1783–1791

71. Alexandridis P (2011) Gold nanoparticle synthesis, morphology control, and stabilization facilitated by functional polymers Chem. Eng Technol 34:15–28

72. Hochbaum AI, Fan R, He R, Yang P (2005) Controlled growth of Si nanowire arrays for device integration. Nano Lett 5:457–460

73. Seo D, Lee J, Kim SW, Kim I, Na J, Hong M-H, Choi H-J (2015) Structural modulation of silicon nanowires by combining a high gas flow rate with metal catalysts. Nanoscale Res Lett 10(190):1–7

74. Hofmann S, Ducati C, Neill RJ, Piscanec S, Ferrari AC, Geng J, Dunin-Borkowski RE, Robertson J (2003) Gold catalyzed growth of silicon nanowires by plasma enhanced chemical vapor deposition. J Appl Phys 94:6005–6012

75. Sujuki H, Araki H, Tosa M, Noda T (2007) Formation of silicon nanowires by CVD using gold catalysts at low temperatures. Mater Transac 48:2202–2206

76. Morales AM, Lieber CM (1998) A laser ablation method for the synthesis of crystalline semiconductor nanowires. Science 279: 208–211

77. Wu S, Shao YM, Nie TX, Xu L, Jiang ZM, Yang XJ (2015) Fabrication of straight silicon nanowires and their conductive properties. Nanoscale Res Lett 10(325):1–8

78. Hibst N, Knittel P, Biskupek J, Kranz C, Mizaikoff B, Strehle S (2016) The mechanisms of platinum-catalyzed silicon nanowire growth. Semicond Sci Tech 31:025005

79. Hasan M, Huq MF, Mahmood ZH (2013) A review on electronic and optical properties of silicon nanowire and its different growth techniques. Springer Plus 2(151):1–9

80. Zhang R-Q, Lifshitz Y, Lee S-T (2003) Oxide-assisted growth of semiconducting nanowires. Adv Mater 15:635–640

81. Yao Y, Li F, Lee S-T (2005) Oriented silicon nanowires on silicon substrates from oxide-assisted growth and gold catalysts. Chem Phys Lett 406:381–385

82. Hutagalung SD, Yaacob KA, Abdul Aziz AF (2007) Oxide-assisted growth of silicon nanowires by carbothermal evaporation. Appl Surf Sci 254:633–637

83. Schmidt V, Wittemann JV, Senz S, Gosele U (2009) Silicon nanowires: a review on aspects of their growth and their electrical properties. Adv Mater 21:2681–2702

84. Schmid H, Bjork MT, Knoch J, Riel H, Riess W (2008) Patterned epitaxial vapor-liquid-solid growth of silicon nanowires on Si (111) using silane. J Appl Phys 103:1–7

85. Christiansen S, Schneider R, Scholz R, Gosele U, Stelzner T, Andra G, Wendler E, Wesch W (2006) Vapor-liquid-solid growth of silicon nanowires by chemical vapor deposition on implanted templates. J Appl Phys 100:1–5

86. Xia Y, Yang P, Sun Y, Wu Y, Mayers B, Gates B, Yin Y, Kim F, Yan H (2003) One-dimensional nanostructures: synthesis, characteristics and applications. Adv Mater 15:353–389

87. Nassiopoulou AG, Gianneta V, Katsogridakis C (2011) Si nanowires by a single-step metal-assisted chemical etching process on lithographically defined areas:formation kinetics. Nanoscale Res Lett 6(597):1–8

88. Osminkina LA, Gonchar KA, Marshov VS, Bunkov KV, Petrov DV, Golovan LA, Talkenberg F, Sivakov VA, Timoshenko VY (2012) Optical properties of silicon nanowire arrays formed by metal-assisted chemical etching: evidences for light localization effect. Nanoscale Res Lett 7:1–6

89. Liu R, Zhang F, Con C, Cui B, Sun B (2013) Lithography-free fabrication of silicon nanowire and nanohole arrays by metal-assisted chemical etching. Nanoscale Res Lett 8:1–8

90. Balasundaram K, Sadhu JS, Shin JC, Azeredo B, Chanda D, Manik M, Hsu K, Rogers JA, Ferreira P, Sinha S, Li X (2012) Porosity control in metal-asisted chemical etching of degenerately doped silicon nanowires. Nanotechnol 23:305304

91. Peng K, Lu A, Zhang R, Lee S-T (2008) Motility of metal nanoparticles in silicon and induced anisotropic silicon etching. Adv Func Mater 18:3026–3035

92. Nassiopoulou AG, Gianneta V, Katsogridakis C (2011) Si nanowires by a single-step metal-assisted chemical etching process on lithographically defined areas: formation kinetics. Nanoscale Res Lett 6:2–8

93. Dawood MK, Tripathy S, Dolmanan SB, Ng TH, Tan H, Lim J (2012) Influence of catalytic gold and silver metal nanoparticles on structural, optical, and vibrational properties of silicon nanowires synthesized by metal-assisted chemical etching. J Appl Phys 112:1–8

94. Pal A, Ghosh R, Giri PK (2015) Early stages of growth of Si nanowires by metal assisted chemical etching: a scaling study. Appl Phys Lett 107:072104

95. Li X (2012) Metal assisted chemical etching for high aspect ratio nanostructures: a review of characteristics and applications in photovoltics. Cur Opin Solid State Mater Sci 16:71–81

96. Peng KQ, Hu JJ, Yan YJ, Wu Y, Feng H, Xu Y (2006) Fabrication of single crystalline silicon nanowires by scratching a silicon surface with catalytic metal particles. Adv Func Mater 16:387–394

97. Peng KQ, Yan YJ, Gao SP, Zhu J (2002) Synthesis of large area silicon nanowire arrays via self assembling nanoelectrochemistry. Adv Mater 14:1164–1167

98. Han H, Huang Z, Lee W (2014) Metal-assisted chemical etching of silicon and nanotechnology applications. Nano Today 9:271–304

99. Lee J-P, Choi S, Park S (2011) Extremely superhydrophobic surfaces with micro- and nanostructures fabricated by copper catalytic etching. Langmuir 27:809–814

100. Asoh H, Arai F, Ono S (2009) Effect of noble metal catalyst species on the morphology of micro porous silicon formed by metal assisted chemical etching. Electrochim Acta 54:5142–5148

101. Chattapadhyay S, Bohn PW (2006) Surfactant-induced modulation of light emission in porous silicon produced by metal-assisted electroless etching. Anal Chem 78:6058–6064

102. Yae S, Morii Y, Fukumuro N, Matsuda H (2012) Catalytic activity of noble metals for metal-aasisted chemical etching of silicon. Nanoscale Res Lett 7:1–5

103. Dimova Malinovaska D, Sendova Vassiliva M, Tzenov N, Kamenova M (1997) Preparation of thin porous silicon layers by stain etching. Thin Solid Films 297:9–12

104. Li X, Bohn PW (2000) Metal-assisted chemical etching in HF/H$_2$O$_2$ produces porous silicon. Appl Phys Lett 77:2572–2574

105. Liu Y, Ji G, Wang J, Liang X, Zuo Z, Shi Y (2012) Fabrication and photocatalytic properties of silicon nanowires by metal-assisted chemical etching: effect of H$_2$O$_2$ concentration. Nanoscale Res Lett 7:1–9

106. Wang D, Ji R, Du S, Albrecht A, Schaaf P (2013) Ordered arrays of nanoporous silicon nanopillars and silicon nanopillars with nanoporous shells. Nanoscale Res Lett 8:1–9

107. Wu S-L, Zhang T, Zheng R-T, Cheng G-A (2012) Facile morphological control of single-crystalline silicon nanowires. Appl Surf Sci 258:9792–9799

108. Li S, Ma W, Zhau Y, Chen X, Xiao Y, Ma M, Zhu W, Wei F (2014) Fabrication of porous silicon nanowires by MACE method in HF/H$_2$O$_2$/AgNO$_3$ system at room temperature. Nanoscale Res Lett 9(196):1–8

109. Lotty O; Petkov, N.; Georgiev, Y. M.; Holmes, J. D. (2012) Porous to nonporous transition in the morphology of metal assisted etched silicon nanowires. Jap J Appl Phys, 51, 11PE03(1–5)

110. Zhang ML, Peng K-Q, Fan X, Jie J-S, Zhang R-Q, Lee S-T, Wong N-B (2008) Preparation of large-area uniform silicon nanowires arrays through metal-assisted chemical etching. J Phys Chem C 112:4444–4450

111. Lee DH, Kim Y, Doerk GS, Laboriante I, Maboudian R (2011) Strategies for controlling Si nanowire formation during Au-assisted electroless etching. J Mater Chem 21:10359–10363

112. Unagami, T. Formation mechanism of porous silicon layer by anodization in HF solution. J Electrochem Soc 1980, 127, 476–483.

113. Kooij ES, Butter K, Kelly JJ (1999) Silicon etching in HNO$_3$/HF solution: charge balance for the oxidation reaction. Electrochem Solid St Lett 2:178

114. Shimizu T, Yamaguchi T, Inoue F, Shingubara S (2012) AgNO$_3$-dependent morphological change of Si nanostructures prepared by single-step metal assisted method. Jpn J Appl Phys 51(11PE02):1–4

115. McSweeney W, Geaney H, O'Dwyer C (2015) Metal assisted chemical etching of silicon and the behavior of nanoscale silicon materials as Li-ion battery anodes. Nano Res 8:1395–1442

116. Zhang T, Zhang P, Li S, Li W, Wu Z, Jiang Y (2013) Black silicon with self-cleaning surface prepared by wetting process. Nanoscale Res Lett 8(351):1–5

117. Chuang CL, Lin JC, Chao KH, Lin CC, Lerondel G (2012) On wet etching of n-Si (100) coated with sparse Ag-particles in aqueous NH$_4$F with the aid of H$_2$O$_2$. Int J Electrochem Sci 7:2947–2964

118. Harada Y, Li XL, Bohn PW, Nuzzo RG (2001) Catalytic amplification of the soft lithographic patterning of Si. Nonelectrochemical orthogonal fabrication of photoluminescent porous Si pixel arrays. J Am Chem Soc 123:8709–8717

119. Bertagna V, Plougonven C, Rouelle F, Chemla M (1996) p- and n-type silicon electrochemical properties in dilute hydrofluoric acid solution. J Electrochem Soc 143:3532–3538

120. Bertagna V, Plougonven C, Rouelle F, Chemla M (1997) Kinetics of electrochemical corrosion of silicon wafers in dilute hydrofluoric solution. J Electroanal Chem 422:115–132

121. Mitsugi N, Nagai K (2004) Pit formation induced by copper contamination on silicon surface immersed in dilute hydrofluoric acid solution. J Electrochem Soc 151:G302–G306

122. Hadjersi T (2007) Oxidizing agent concentration effect on metal-assisted electroless etching mechanism in HF-oxidizing agent-H$_2$O solutions. Appl Surf Sci 253:4156–4160

123. Peng K, Fang H, Hu J, Wu Y, Zhu J, Yan Y, Lee ST (2006) Metal-particle-induced, highly localized site-specific etching of Si and formation of single-crystalline Si nanowires in aqueous fluoride solution. Chem Eur J 12:7942–7947

124. Ono S, Oide A, Asoh H (2007) Nanopatterning of silicon with use of self-organized porous alumina and colloidal crystals as mask. Electrochim Acta 52:2898–2904

125. Asoh H, Sakamoto S, Ono S (2007) Metal patterning on silicon surface by site-selective electroless deposition through colloidal crystal templating. J Colloid Interface Sci 316:547–552

126. Huang Z, Geyer N, Werner P, Boor JD, Gosele U (2011) Metal-assisted chemical etching of Si: a review. Adv Mater 23:285–308

127. Song YY, Gao ZD, Kelly JJ, Xia XH (2005) Galvanic deposition of nanostructured Noble-metal films on silicon. Electrochem Solid State Lett 8:C148–C150

128. Qiu T, Wu XL, Siu GG, Chu PK (2006) Intergrowth mechanism of silicon nanowires and silver dendrites. J Electron Mater 35:1879–1884

129. Goszner K, Bischof H (1974) The decomposition of hydrogen peroxide on silver—gold alloys. J Catal 32:175–182

130. Kooij ES, Butter K, Kelley JJ (1999) Silicon etching in HNO$_3$/HF solution: charge balance for the oxidation reaction. Electrochem Solid State Lett 2:178–180

131. Turner DR (1960) On the mechanism of chemically etching germanium and silicon. J Electrochem Soc 107:810–816

132. Nahm KS, Seo YH, Lee HJ (1997) Formation mechanism of stains during Si etching reaction in HF–oxidizing agent–H$_2$O solutions. J Appl Phys 81:2418–2424

133. Chen, Q. W.; Li, X. J.; Zhang, Y. H. Material synthesis: microstructure and light emitting in porous silicon derived from hydrothermal etching. High Pressure Res 2001, 20, 1–8.

134. Nahidi M, Kolasinski KW (2006) Effects of stain etchant composition on the photoluminescence and morphology of porous silicon. Electrochemical/chemical deposition and etching. J Elctrochem Soc 153:C19–C26

135. Seidel, H.; Csepregi, L.; Heuberger, A.H.;Baumgartel, A. Anisotropic etching of crystalline silicon in alkaline solutions. J Electrochem Soc 1990, 137, 3613–3626.

136. Li Y, Duan C (2015) Bubble-regulated silicon nanowire synthesis on micro-structured surfaces by metal-assisted chemical etching. Langmuir 31:12291–12299

137. Qiu T, Wu XL, Mie YF, Wan GJ, Chu PK, Siu GG (2005) Si nanotubes to nanowires: synthesis, characterization and self assembly. J Crys Growth 277:143–148

138. Peng K, Yan Y, Gao S, Zhu J (2003) Dendrite-assisted growth of silicon nanowires in electroless metal deposition. Adv Func Mater 13:127–132

139. Chattopadhyay S, Bohn PW (2004) Direct-write patterning of microstructured porous silicon arrays by focused-ion-beam Pt deposition and metal-assisted electroless etching. J Appl Phys 96:6888–6894

140. Kayes BM, Filler MA, Putnam MC, Kelzenberg MD, Lewis NS, Atwater HA (2007) Growth of vertically aligned Si wire arrays over large areas (>1 cm^2) with Au and Cu catalysts. Appl Phys Lett 91(103110):1–3

141. Huang Z, Zhang X, Reiche M, Liu L, Lee W, Shimizu T, Senz S, Gosele U (2008) Extended array of vertically aligned sub-10 nm diameter [100] Si nanowires by metal-assisted chemical etching. Nano Lett 8:3046–3051

142. Kim J, Han H, Kim YH, Choi S-H, Kim J-C, Lee W (2011) Au/Ag bilayered metal mesh as a Si etching catalyst for controlled fabrication of Si nanowires. ACS Nano 5:3222–3229

143. Kim J, Kim YH, Choi S-H, Lee W (2011) Curved silicon nanowires with ribbon-like cross section by metal-assisted chemical etching. ACS Nano 5:5242–5248

144. Huang Z, Fang H, Zhu J (2007) Fabrication of silicon nanowire arrays with controlled diameter, length and density. Adv Mater 19:744–748

145. Chang S-W, Chuang VP, Boles ST, Ross CA, Thompson CV (2009) Densely packed arrays of ultra-high-aspect-ratio silicon nanowires fabricated using block-copolymer lithography and metal-assisted etching. Adv Func Mater 19:2495–2500

146. Choi WK, Liew TH, Dawood MK, Smith HI, Thompson CV, Hong MH (2008) Synthesis of silicon nanowires and nanofin arrays using interference lithography and catalytic etching. Nano Lett 8:3799–3802

147. Premasiri WR, Clarke RH, Womble ME (2001) Urine analysis by laser Raman spectroscopy. Lasers Surg Med 28:330–334

148. Li T, Guo L, Wang Z (2008) Gold nanoparticle-based surface enhanced Raman spectroscopic assay for the detection of protein-protein interactions. Anal Sci 24:907–910

149. Fazio B, D'Andrea C, Foti A, Messina E, Irrera A, Donato MG, Villari V, Micali N, Maragò OM, Gucciardi PG (2016) SERS detection of biomolecules at physiological pH via aggregation of gold nanorods mediated by optical forces and plasmonic heating. Sci Rep 6(26952):1–13

150. Kneipp K, Yang Y, Kneipp H, Perelman LT, Itzkan I, Dasari RR, Feld MS (1997) Single-molecule detection using surface-enhanced Raman scattering (SERS). Phys Rev Lett 78:1667–1670

151. Nie S, Emory SR (1997) Probing single molecules and single nanoparticles by surface-enhanced Raman scattering. Science 275:1102–1106

152. Jiang ZY, Jiang XX, Su S, Wei XP, Lee ST, He Y (2012) Silicon-based reproducible and active surface-enhanced Raman scattering substrates for sensitive, specific, and multiplex DNA detection. Appl Phys Lett 100(203104):1–4

153. Liu B, Lin M, Li H (2010) Potential of SERS for rapid detection of melamine and cyanuric acid extracted from milk. Sens Instrument Food Qual 4:13–19

154. Castillo F, Perez E, de la Rosa E (2011) Adsorption of gold nanoparticles on silicon substrate and their application in surface enhanced Raman scattering. Revista Maxicana de Fisica S57:61–65

155. Cerf A, Molnar G, Vieu C (2009) Novel approach for the assembly of highly efficient SERS substrate. Appl Mater Interface 1:2544–2550

156. Gunnarsson L, Bjerneld EJ, Xu H, Petronis S, Kasemo B, Kall M (2001) Interparticle coupling effects in nanofabricated substrates for surface-enhanced Raman scattering. Appl Phys Lett 78:802–804

157. Peters RF, Gutierrez-Rivera L, Dew SK, Stepanova M (2015) Surface enhanced Raman spectroscopy detection of biomolecules using EBL fabricated nanostructured substrates. J Vis Exp 97:1–17

158. Alvarez-Puebla R, Cui B, Bravo-Vasquez J-P, Veres T, Fenniri H (2007) Nanoimprinted SERS-active substrates with tunable surface Plasmon resonances. J Phys Chem C 111:6720–6723

159. Chou SY, Krauss PR, Renstrom PJ (1995) Imprint of sub 25 nm vias and trenches in polymers. Appl Phys Lett 67:3114–3116

160. Wang Y, Wang W, Liu L, Feng L, Zeng Z, Li H, Xu W, Wu Z, Hu W et al (2013) Highly effective and reproducible surface-enhanced Raman scattering substrates based on Ag pyramidal arrays. Nano Res 6:159–166

161. Li M, Zhao F, Zeng J, Qi J, Lu J, Shih WC (2014) Microfluidic surface-enhanced Raman scattering sensor with monolithically integrated nanoporous gold disk arrays for rapid and label-free biomolecular detection. J Biomed Opt 19(111611):1–8

162. Bronstrup G, Jahr N, Leiterer C, Csaki A, Fritzsche W (2010) Optical properties of individual silicon nanowires for photonic devices. ACS Nano 4:7113–7122

163. Yin J, Qi X, Yang L, Hao G, Li J, Zhong J (2011) A hydrogen peroxide electrochemical sensor based on silver nanoparticles decorated silicon nanowire arrays. Electrochim Acta 56:3884–3889

164. Wang XT, Shi WS, She GW, Mu LX, Lee ST (2010) High-performance surface-enhanced Raman scattering sensors based on Ag nanoparticles-coated Si nanowire arrays for quantitative detection of pesticides. Appl Phys Lett 96:053104

165. Luong TQN, Cao TA, Dao TC (2013) Low-concentration organic molecules detection via surface-enhanced Raman spectroscopy effect using Ag nanoparticles-coated silicon nanowire arrays. Adv Nat Sci Nanosci Nanotechnol 4:015018

166. He Y, Su S, Xu T, Zhong Y, Zapien JA, Li J, Fan C, Lee S-T (2011) Silicon nanowires-based highly-efficient SERS-active platform for ultrasensitive DNA detection. Nano Today 6:122–130

167. Zhang B, Wang H, Lu L, Ai K, Zhang G, Cheng X (2008) Large-area silver-coated silicon nanowire array for molecular sensing using surface-enhanced Raman spectroscopy. Adv Func Mater 18:2348–2355

168. Peng KQ, Wu Y, Fang H, Zhong XY, Xu Y, Zhu JA (2005) Uniform, axial-orientation alignment of onedimensional single-crystal silicon nanostructure arrays. Angew Chem Int Ed 44:2737–2742

169. Yi C, Li C-W, Fu H, Zhang M, Qi S, Wong N-B, Lee S-T, Yang M (2010) Patterned growth of vertically aligned nanowire arrays for level-free DNA detection using surface-enhanced Raman spectroscopy. Anal Bioanal Chem 397:3143–3150

170. Wang H, Han X, Ou X, Lee C-S, Zhang X, Lee S-T (2013) Silicon nanowire based single-molecule SERS sensor. Nano 5:8172–8176